Construction and Building Materials 195 (2019) 650–670

Contents lists available at ScienceDirect

Construction and Building Materials

journal homepage: www.elsevier.com/locate/conbuildmat

Experimental response of URM single leaf and cavity walls in out-of-plane two-way bending generated by seismic excitation

F. Graziotti [a,b,*], U. Tomassetti [a,b], S. Sharma [b,c], L. Grottoli [b], G. Magenes [a,b]

[a] Dept. of Civil Engineering and Architecture – DICAr, University of Pavia, Italy
[b] European Centre for Training and Research in Earthquake Engineering – EUCENTRE, Pavia, Italy
[c] UME School, Istituto Universitario di Studi Superiori – IUSS, Pavia, Italy

HIGHLIGHTS

- Results of the first dynamic tests of full-scale URM walls subjected to OOP 2WB.
- Results in terms of deformed shapes, failure mechanisms and force-displacement hysteretic curves.
- Characterisation test to evaluate the response of URM under torsional shear.
- Application of analytical techniques based on virtual method.

ARTICLE INFO

Article history:
Received 16 May 2018
Received in revised form 11 October 2018
Accepted 12 October 2018
Available online 26 November 2018

Keywords:
Full-scale shaking table test
Two-way bending
Out-of-plane
Cavity wall
URM
Torsional strength
Virtual work method

ABSTRACT

Out-of-plane (OOP) mechanisms are one of the major causes of structural collapse in unreinforced masonry (URM) buildings as observed in recent as well as past seismic events. Among such failures, two-way bending mechanisms involving at least one restrained vertical edge constitute a very distinct majority. Nevertheless, very little research pertaining to such mechanisms can be found currently in literature. The paper takes a step forward in this topic through the execution and interpretation of dynamic tests on four full-scale single leaf and one full-scale cavity URM walls. Each tested full-scale specimen consisting of a OOP panel and two return walls, varying in terms of commonly encountered boundary conditions, applied overburden or the presence/absence of an opening. The specimens were subjected to sequences of incremental input motion till collapse and these results are presented in terms of deformed shapes, failure mechanisms and force-displacement hysteretic curves. State of the art analytical techniques based on the method of virtual work are applied to evaluate their reliability as simplified tools for assessing the behaviour of such wall subjected to OOP two-way bending excitation. The testing campaign resulted in all specimens exhibiting a rather brittle response, despite sustaining accelerations of 1 g without any damage.

1. Introduction

Vulnerability to out-of-plane (OOP) dynamic excitation represents one of the most important aspects of URM structures subjected to seismic loading. OOP failures have been widely reported by damage observations in the aftermath of recent as well as past earthquakes to be an important cause of structural collapse [1–5]. Considering OOP failures, a distinction can be made between: vertical (or one-way) bending of the wall occurring in longer walls and walls without side supports; two-way bending in walls with at least one vertical edge supported; top portion cantilever type failure with the entire top section of a wall or building facade collapsing.

While the need to address OOP failure in URM has generated significant interest, most of the research until now has solely focused on the one-way bending mechanism. Such studies include both detailed experimental studies on walls alone [6–10], walls in buildings [11] and numerical analyses [12–14]. Such studies have shown that OOP failures are due to attainment of displacement levels incompatible with equilibrium configurations of the considered mechanism rather than the exceedance of stress capacity in structural elements.

Research on the two-way bending mechanism is instead limited to quasi-static airbag tests on full-scale specimens [15–17], inclined platform [18] and dynamic shaking table tests on half-scale specimens [19]. This is despite the fact that support condi-

* Corresponding author.
E-mail addresses: francesco.graziotti@unipv.it (F. Graziotti), umberto.tomassetti01@universitadipavia.it (U. Tomassetti), satyadhrik.sharma@iusspavia.it (S. Sharma), luca.grottoli@eucentre.it (L. Grottoli), guido.magenes@unipv.it (G. Magenes).

https://doi.org/10.1016/j.conbuildmat.2018.10.076
0950-0618/

tions (walls having one or both vertical edges supported) leading to two-way bending are very commonly encountered. In fact, following the Christchurch earthquakes, Dizhur et al. [20] estimated two-way bending to be the responsible failure mechanism in almost 57% of cases while one-way bending and top portion cantilever-type failure accounted for 7% and 36% respectively.

Consequently, an experimental campaign addressing the dynamic behaviour of URM walls subjected to both horizontal and vertical bending was programmed and designed at the EUCENTRE laboratory of Pavia. This research was performed within the framework of a wider project aiming at assessing the vulnerability of URM building in the province of Groningen: a region of Netherlands not naturally prone to seismic events but exposed to induced seismicity. The URM building stock in Groningen also presents several peculiarities in commonly adopted structural solutions which include flexible diaphragms, cavity walls, high slenderness of piers, lack of effective diaphragm to wall connections and very large openings. Activities carried out within the framework of the research project include (but are not limited to): in situ and laboratory mechanical characterization tests performed on bricks, mortar and small masonry assemblies, in-plane cyclic shear-compression on full-scale masonry piers [21]; dynamic OOP one-way bending tests [7] together with several shaking table tests conducted on full-scale URM buildings (e.g. [22–25]) to study their global seismic behaviour. A comprehensive review of the experimental campaign until now can be found in Graziotti et al. [26].

Most current building standards (including the one used in the Groningen province [27]) ignore the presence of vertical supports and does not consider two-way bending mechanisms. However, ignoring the enhancement of strength as well as the modification of displacement capacities due to restraint at vertical edges can lead to overtly conservative results. In this context, it is very interesting to note that this is the first experimental campaign, to the authors' knowledge, addressing the dynamic response and collapse of full-scale URM walls in the OOP direction and under two-way bending. Keeping this along with the costs associated with full-scale dynamic testing in mind, the entire experimental programme was designed specifically not only to improve understanding of the mechanisms involved but also to aid and develop capabilities to model such behaviour analytically or numerically. This experimental campaign was also expected to provide valuable insights into the comparison between results observed for wall specimens with that of local two-way-bending failures observed in full-scale building prototypes (e.g. [24]).

This paper initially presents the U-shaped URM specimens tested and their material characterisation. The test setup, instrumentation, input motions and their sequence adopted for incremental dynamic testing are then illustrated in detail. Results of the tests are then presented in terms of observed damage and failure mechanisms, deformed shapes and force-displacement hysteresis curves. Emphasis is then placed at utilising methods ranging from those available in building codes to practitioners to state of the art analytical methods in literature in an attempt to evaluate their reliability towards predicting and understanding the behaviour of these walls. The testing of five full-scale specimens has been completed at this phase in the project and the testing of more full-scale specimens is envisaged (varying material properties, boundary conditions and seismic input) in the near future.

2. Description and mechanical characterisation of the masonry specimens

2.1. Specimen geometries

Each tested specimen had a U-shaped plan, consisting of two 1-m-long return walls restraining a 4-m-long OOP panel on the two lateral vertical edges. Connection between the OOP panel and return walls consisted of alternating rows of headers from the OOP panel and stretchers from the return walls, providing a full moment connection at the vertical edges. Materials of the specimens were chosen to represent typical constructions in Groningen province. The first three specimens corresponded to 100-mm-thick single leaf walls constructed with Calcium Silicate (CS) bricks measuring 212 × 102 × 71 mm while the fourth specimen was a single leaf wall constructed with clay bricks measuring 208 × 98 × 50 mm. Additionally, the third CS specimen had an opening which was located eccentrically. The CS walls were all constructed in 34 layers of bricks while the clay brick walls in 46 layers. Since all masonry joints were 10-mm thick, this corresponded to a total height of 2.75 m and 2.76 m for the CS and clay brick specimens respectively (Fig. 1).

The fifth specimen was a cavity wall with an outer leaf constructed with clay bricks and the inner leaf with CS bricks (having the same geometry as the first three specimens). Correspondingly, this specimen had four return walls, two per leaf. L-shaped metal connectors at a density of 2 ties/m^2 were used to connect the two masonry leaves. Table 1 specifies the specimens' name adopted throughout the rest of the article along with the OOP panel mass, boundary conditions and applied overburden pressure.

The OOP panel of the first specimen (*i.e.* tests CS-010-RR and CS-005-RR) was initially subjected to a vertical overburden stress value (σ_v) equal to 0.10 MPa. This was later decreased to 0.05 MPa in order to reduce the horizontal and diagonal bending strength and consequently decrease the inertial force required to induce cracking. The resulting initial static scheme was double fixed in both, vertical and horizontal edges for both specimen configurations CS-010-RR and CS-005-RR. It should be noted that a vertical overburden pressure, equal to 0.05 MPa, was applied on the top of the return walls regardless of the boundary conditions associated with the OOP panel. Idealized initial boundary conditions were envisaged in this experimental campaign as the motive was to develop an experimental database with which numerical models could be developed and calibrated. Such boundary conditions may not be representative of all the configurations in the building stock. Nevertheless, the applied level of imposed vertical overburden pressure can be considered similar to that of a loadbearing wall located on the second floor of a typical two-storeyed URM residential building with RC slab. The OOP panel of all other specimens was unloaded with the top horizontal edge kept free. This led to a fixed-free restraint scheme in the vertical spanning direction. Such specimens can be considered somehow representative of walls located at the top storey of a building and parallel to the spanning direction of the roof diaphragm and without any proper connection between the wall and the roof. Additionally, these boundary conditions may also arise due to interaction with other structural elements during the dynamic response of a building. For example, in a shaking table test performed as part of the same project, Tomassetti et al. [24] highlighted that the OOP collapse of a flange wall may be induced by the pronounced in-plane rocking behaviour of its perpendicular walls. Such rocking behaviour caused the uplift of the supported rigid floor slab, leading to the loss of restraint and axial load transfer at the top of the OOP panel. Similar behaviour was also observed in a shaking table test performed by Beyer et al. [11] on a mixed RC/URM building.

2.2. Summary of masonry mechanical properties

All specimens tested on shake table were accompanied by complementary detailed material characterisation on both constituents as well as masonry as a composite. Table 2 summarizes experimental mean values and coefficient of variation (*C.o.V.*) for the

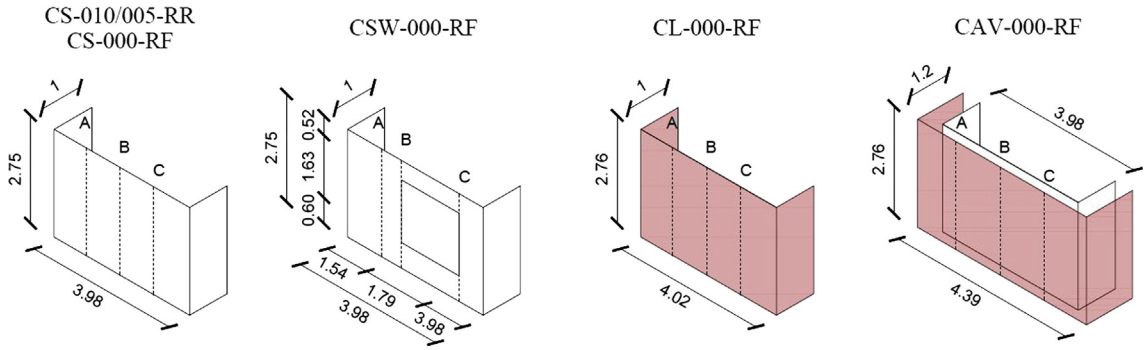

Fig. 1. Specimen geometries (dimensions in m).

Table 1
Test specimens: boundary conditions and applied overburden pressure.

Specimen		l_{OOP} [m]	h_{OOP} [m]	M [kg]	σ_v OOP wall [MPa]	σ_v RET wall [MPa]	Horizontal restrain condition	Scheme
CS-010-RR		3.98	2.75	2056	0.10	0.10	Fixed (R) Fixed (R)	
CS-005-RR		3.98	2.75	2056	0.05	0.05	Fixed (R) Fixed (R)	
CS-000-RF		3.98	2.75	2056	-	0.05	Fixed (R) Free (F)	
CSW-000-RF		3.98	2.75	1530	-	0.05	Fixed (R) Free (F)	
CL-000-RF		4.02	2.76	2178	-	0.05	Fixed (R) Free (F)	
CAV-000-RF	CS	3.98	2.75	2056	-	0.05	Fixed (R) Free (F)	
	Clay	4.39	2.76	2375	-	0.05	Fixed (R) Free (F)	

investigated mechanical parameters: namely Young's Modulus in compression (E), compressive strength (f_m) and flexural tensile strength of masonry perpendicular (f_{mt}) to bed-joints, compressive (f_c) and flexural strength (f_t) of mortar, compressive (f_u) and tensile (f_{ut}) strength of bricks and initial shear strength and friction coefficient of masonry bed joints under direct (f_{v0} and μ) shear. All tests were performed in compliance with the latest applicable European norms [28–32]. In order to characterise the response of masonry bed joints under torsional shear stress ($f_{v0,tor}$ and μ_{tor}), an additional test was performed. More details about this test are provided in Section 2.3. The average pull-out/push-in strengths associated with this tie typology in CS and Clay URM specimens are approximately 1.25/1.13 kN and 1.94/1.78 kN respectively, while the ultimate tensile capacity of the ties is approximately 4.3 kN [33].

2.3. Characterisation of the torsional shear strength of bed joints in masonry

URM masonry under two-way bending and generally when subjected to flexure about an axis normal to its bed joint bending derives a considerable portion of its resistance from the torsional shear capacity of bed joints [34]. Although the large amount of research on the behaviour of URM under the action of uniform shear stress at the brick mortar interface, very limited research exists on the response of bed joints in masonry under torsional shear where the distribution of shear stress is non-uniform. This is despite the fact that torsional shear resistance is one of the most important controlling parameters in virtual work based methods [35] that constitute existing state of the art analytical formulation applied to URM loaded in the OOP direction. Consequently, a novel characterisation test was planned in order to evaluate the response of masonry bed joints under combined torsion and compression. More details about how the results of this test were used to understand the behaviour of the dynamically tested specimens are provided in Section 5.

Specimens tested consisted of two units bonded together by a mortar bed joint reduced in area to 100 × 100 mm, representative of the overlap that occurs between bricks in adjacent courses of the full-scale walls. The bottom unit was clamped and restrained from any possible movement with the help of steel profiles bolted to the test setup. A hydraulic jack was used to apply vertical pre-compression on the top of the upper brick through a thick steel plate to ensure a proper distribution of the applied stress. A sheet of flexible elastomer was placed between the upper brick and this steel plate to allow possible dilatancy to occur maintaining the vertical compression almost constant. Torsional shear stress in the

Table 2
Summary of material characterization tests of masonry.

			E	f_m	f_{mt}	f_c	f_t	f_u	f_{ut}	f_{v0}	μ	$f_{v0,tor}$	μ_{tor}
CS	*Mean*	[MPa]	4784	9.74	0.95	8.49	2.72	15.31	2.61	0.81	0.46	1.86	1.20
	C.o.V.	[%]	18.0	7.8	18.2	32.9	31.3	6.1	14.5	–	–	–	–
Clay	*Mean*	[MPa]	7497	17.41	0.41	4.51	1.15	46.80	7.83	0.18	0.63	1.13	1.63
	C.o.V.	[%]	26.3	8.5	55.3	12.5	15.8	10.9	4.7	–	–	–	–

bed joint was induced by two hydraulic jacks connected to the same circuit and hence applying the same pressure. This resulted in gradually increasing horizontal loads on steel triangular prisms attached to the bricks at a fixed distance from their ends forming a force couple. These horizontal forces were increased gradually up to failure of the bed joint was observed after which they were increased once again after changing the applied vertical pre-compression to obtain data on the post-peak residual behaviour. Horizontal displacements at both brick edges as well as vertical displacements were monitored using potentiometers. A schematic of how this test was performed and an image of the setup in the laboratory can be seen in Fig. 2a and b. Failure in CS masonry consisted of a crack through the mortar joint which then proceeded to the brick-mortar interface while for clay masonry, the failure always occurred only in the brick-mortar interface (Fig. 2c and d).

In order to evaluate the torsional shear strength of a masonry bed joint from these results, the mortar joint was idealised as an elastic rectangular shaft having dimensions a, b (equal to 100 mm for both Clay and CS) and height equal to thickness of the joint. Such an idealisation was adopted as it can be observed that the specimens exhibited linear elastic behaviour until ultimate torque was reached (Fig. 3a). From the ultimate torque (T_{max}) measured experimentally, the torsional shear strength of the bed joint (τ_{tor}) was computed as:

$$\tau_{tor} = \frac{T_{max}(3a + 1.8b)}{a^2 b^2} = 4800\ [\mathrm{m}^{-3}] \cdot T_{max} \quad (1)$$

The constant part of this expression depends on the geometry of the rectangular shaft (the mortar joint here) and is dependent on the adopted stress distribution in the cross-section of the shaft *i.e.* maximum shear stress occurs at the centre of the longer side [36], here the shear stress at the centre of all sides is expected to be similar since the tested mortar joint is square. Similar to the prescriptions of the relevant European norm while evaluating the initial shear strength of masonry bed joints under translational shear [32], these specimens were also tested under different levels of vertical pre-compression: 0.1 MPa, 0.2 MPa, 0.4 MPa and 0.6 MPa. Higher pre-compression was not applied as it resulted in the failure of units along with shear failure of the bed joints. The results of this test were also represented in a Coulomb-type friction law representation after performing linear regression in order to obtain corresponding values of initial shear strength ($f_{v0,tor}$) and coefficient of friction (μ_{tor}) under torsional shear (Fig. 3b). Despite the dispersion observed in the results (particularly for CS masonry), it is interesting to note that similar values of coefficient of friction are calculated when computing a Coulomb-type friction law for the residual torsional shear strength of masonry. The Coulomb-type friction laws reported here correspond to ten clay and thirteen CS specimens.

3. Testing layout and applied testing sequences

3.1. Testing setup

The specimens were anchored to the shake table through the reinforced concrete (RC) foundation by means of steel bolts. The bottom section of the specimens lay on a mortar bed-joint resting on the foundation, achieving the fixed boundary condition at the bottom. Two return walls ensured moment restraint at both the vertical edges of the OOP panel. A rigid steel frame was installed to transfer the input from the shaking table to the top of the wall. This frame was connected to a steel beam on top of the wall by four steel braces with mechanical hinges at one end (the extremity connected to the frame). Rigidly bolted connections at the other extremity prevented any relative rotations of this beam with respect to the bracing system. This system, shown in Fig. 4a and b, allowed any uplift of the wall while simultaneously transferring the horizontal dynamic input of the shake table to the top of the specimen with low acceleration amplification. The acceleration spectra at top of the walls were slightly amplified around the natural frequency of the steel frame (≈25 Hz). This resulted in an overshoot of around 30% for CS-005-RR at the undamaged natural frequency of the specimen (22.9 Hz). For all other specimens, the acceleration spectra deviated less than 10% from the applied input in the bandwidth 0–20 Hz representing their frequency range of interest (Section 4.1).

Vertical pre-compression was applied to the OOP panel in case of the first specimen (CS-010-RR) by pulling down the top beam by means of 4 steel hollow cantilevers bolted to the web of the top beam which were connected to bars in series with a system of springs. The stiffness of the spring system was chosen to ensure that the increase in force at collapse is less than 5% of the initial static pre-compression. This simplified calculation was performed taking into account the maximum uplift demand of a rigid-body one-way bending collapse mechanism though the actual uplift was recorded to be significantly lower. Springs having a stiffness of 53.5 N/mm were ultimately used to provide both 0.10 MPa and 0.05 MPa of vertical overburden.

A similar system was used to load the return walls in case of all other specimens (Figs. 4d and e and 5c–e). For the first specimen, the horizontal restraint (fixed) condition on the top of the OOP panel was guaranteed by L-shaped steel profiles bolted to the bottom of the top beam and clamping the top layer of bricks Additionally, high strength mortar was used to fill the gap between the top row of bricks and the steel profiles (Fig. 4b). For all other speci-

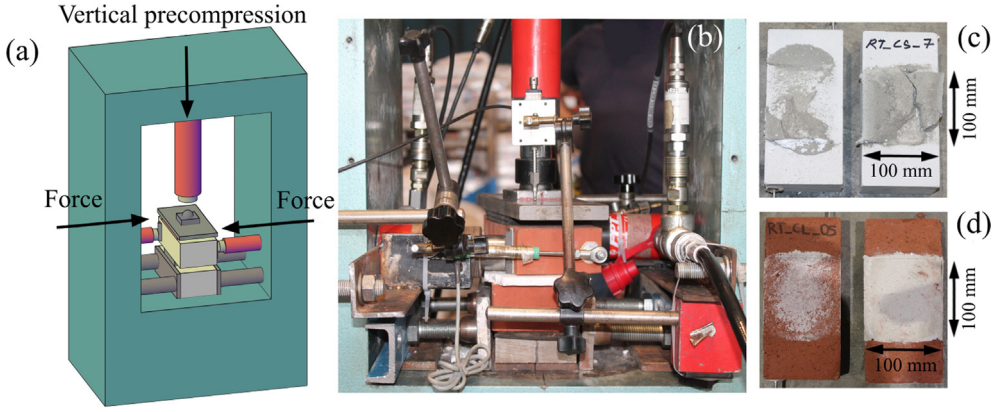

Fig. 2. Setup for testing the torsional shear strength of bed joints (a and b) and failure modes occurring in the specimens (c and d).

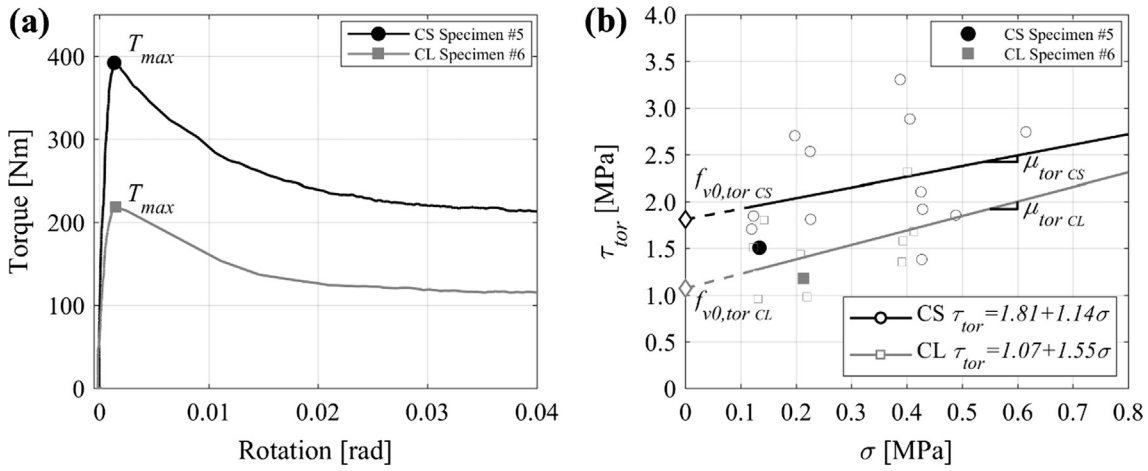

Fig. 3. Typical torque-rotation behaviour of CS and CL specimens (a) and Coulomb type friction law representation of results (b).

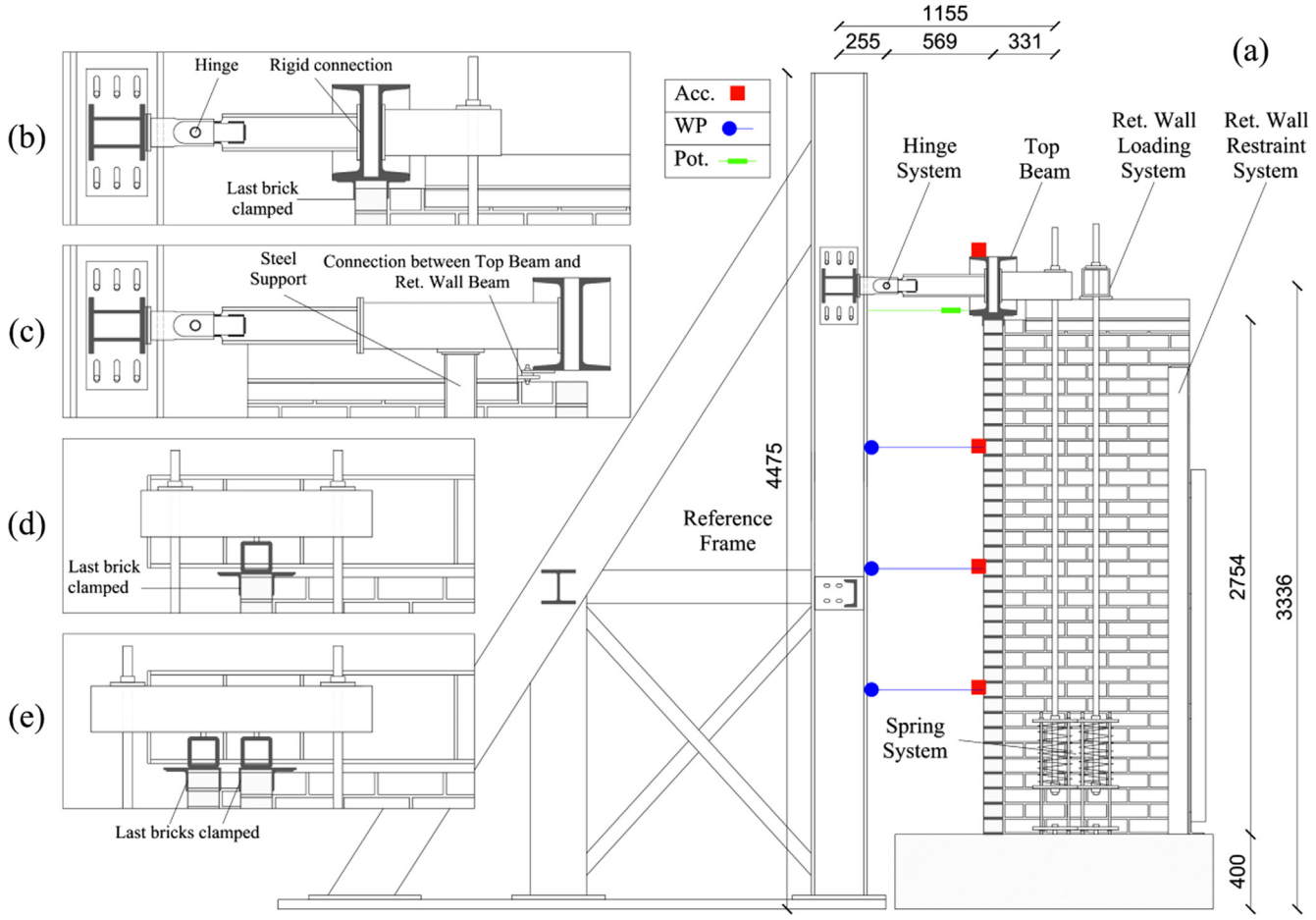

Fig. 4. Overall geometry of the test set-up (a), connection between top beam and rigid frame in case of CS-010/005-RR (b) and all other specimens, (c); fixity of the return wall top for single leaf (d) and cavity (e) specimens (dimensions in mm).

mens, the OOP panel was unloaded and hence the top beam was lifted by steel supports in order to maintain a 30 mm air gap between the top row of bricks and the bottom edge of the top beam. Four steel plates (two per return wall) ensured the rigidity of the connection between the OOP panel top beam and the top beam for loading the return walls (Figs. 4c and 5g). This allowed for the transmission of the input acceleration also to the upper portion of the return walls, even in the case of OOP panels being free on top. Steel profiles were also used to clamp the free extremities of the return walls (Fig. 5c and d) to prevent any possible OOP displacement transverse to the direction of input motion. Minor changes in terms of dimensions had to be made to the test setup in order to accommodate the cavity wall and when the entire setup was rotated to accommodate better recording of displacements using an optical acquisition system from the second specimen onwards (from Fig. 5b to Fig. 5a configuration and Fig. 5f).

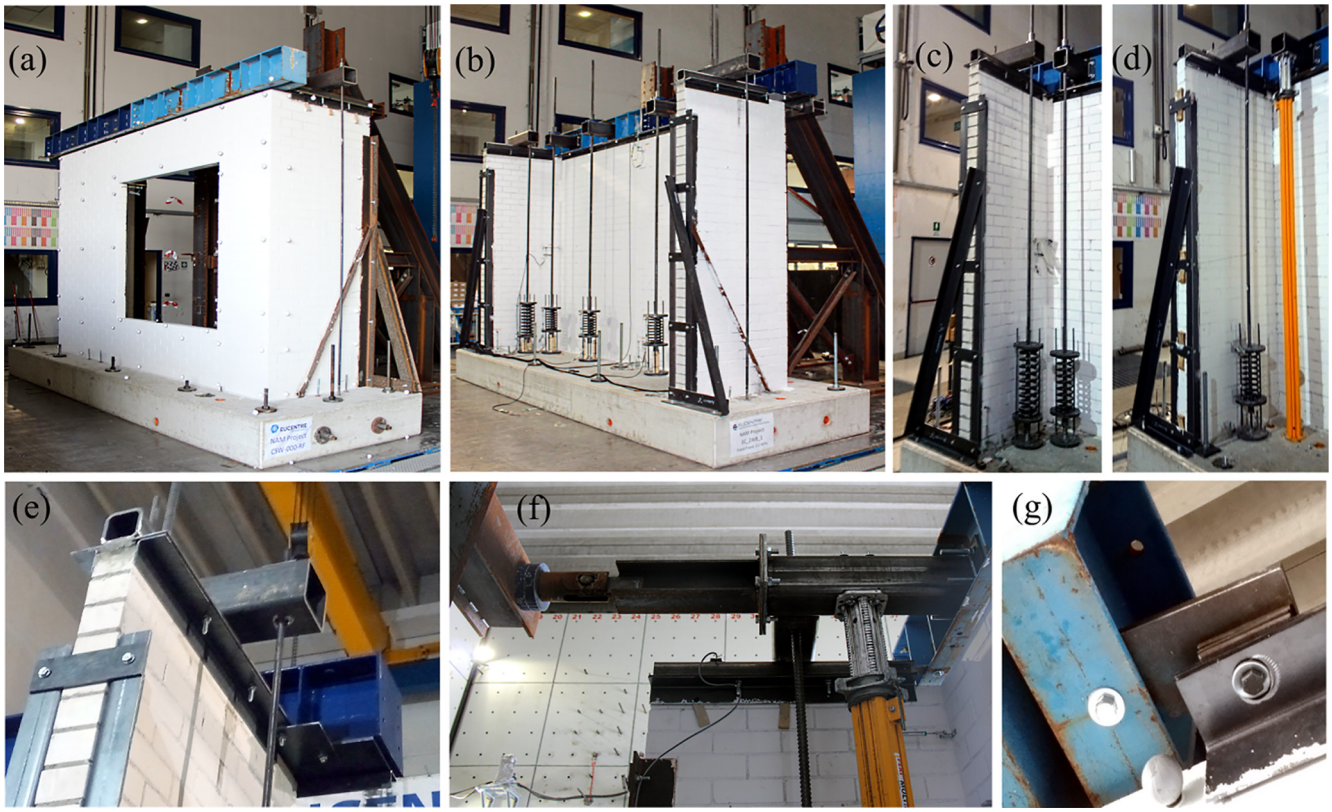

Fig. 5. Testing layout: general view of CSW-000-RF (a) and CS-005-RR (b) testing setup, spring system for the application of the top overburden pressure (c), support for the uplift of the top beam in case of CS-000-RF (d); fixity of the top of return walls (e), elongation of connection between rigid frame and top beam (f), connection between the top beam and beam above the return walls (g).

3.2. Instrumentation and data acquisition

The instrumentation adopted for each specimen consisted of accelerometers, potentiometers, wire potentiometers and a 3D optical acquisition system (used for all specimens barring the first one). The location of all the instrumentation adopted for each specimen was decided based on the boundary conditions envisaged and correspondingly expected deformed shapes. Accelerometers were installed on the OOP panel of the specimen in order to record acceleration-time histories. Additional accelerometers were also installed at the specimen foundation, top beam, rigid frame and the return walls. Potentiometers were used to measure relative displacements associated with various locations of the specimen. Wire potentiometers attached to the rigid frame in several locations were used to record horizontal displacements relative to the shake table. Some potentiometers were also adopted to record the relative displacements between the main panel and the return walls. All experimental data [37] along with detailed descriptions and illustrations of instrumentation [38] adopted for each of the specimens are freely available upon request from www.eucentre.it/nam-project.

3.3. Input signals and testing sequence

Incremental dynamic tests, *i.e.* a series of table motions of increasing intensity, were performed on each specimen to fully exploit their horizontal load carrying capacity. The input sequence employed was the same as that performed by Graziotti et al. [22]. This was done to facilitate comparison between results observed for the wall specimens with that of a full-scale building prototype in which second and first-storey transverse walls were excited in the OOP direction. Primarily three input motions were used throughout the entire testing sequence: FHUIZ-DS0, FEQ2-DS3 and FEQ2-DS4. FHUIZ-DS0 was the second floor accelerogram obtained from a calibrated TREMURI [39] model of the tested full-scale house (in an undamaged configuration) when subjected to the ground motion recorded at Huizinge, The Netherlands on 16th April 2012 [40]. This represents the largest magnitude event which has occurred in Groningen field until now. FEQ2-DS3 and FEQ2-DS4 correspond to recorded second floor accelerograms of the full-scale house when subjected to ground motion EQ2 scaled up to 125% and 200%, respectively. The ground motion EQ2 was obtained from a 2015 hazard study of the Groningen province and can be deemed representative of the dynamic characteristics of the induced seismicity with an associated *PGA* of 0.16 g [41]. These two acceleration histories (FEQ2-DS3 and FEQ2-DS4) can be considered well representative of the progressive damage evolution between DS3/Moderate Damage and DS4/Extensive Damage which occurred in the house [22].

A fourth artificial input signal, characterized by a wide spectral shape and long duration, was adopted only in order to induce a collapse of the first specimen while avoiding the unrealistic scaling of the experimental floor motions. This input signal consisted of a sequence of sine impulses with gradually increasing periods in order to excite a wide range of frequencies in the specimen. It should also be noted that the specimens were subjected to low amplitude random excitations (RN) in order to identify their dynamic properties in between test runs. Low intensity calibration runs were also performed in order to have a better control of the shaking table.

Table 3 specifies the adopted input floor motions and the ground motions they have been obtained from together with the associated *PGA*. Other intensity measures including peak table acceleration, velocity and displacement (*PTA*, *PTV* and *PTD*) as well as cumulative absolute velocity (*CAV*), Arias intensity (I_A) and modified Housner intensity (*mHI*, integrated between periods 0.1 s and

Table 3
Characteristics of employed input motions at scaling factor equal to 1.

Input	Description	GM input	GM *PGA* [g]	*PTA* [g]	*PTD* [mm]	*PTV* [mm/s]	I_A [mm/s]	*mHI* [mm]	*CAV* [m/s]	*DS* [s]
FHUIZ-DS0	2nd Floor Acc. (Numerical)	Huizinge	0.08	0.15	4.3	47	47.6	35.5	0.90	0.52
FEQ2-DS3	2nd Floor Acc. (Experimental)	EQ2-125%	0.19	0.26	25.7	181	399	112.2	3.72	1.83
FEQ2-DS4	2nd Floor Acc. (Experimental)	EQ2-200%	0.31	0.32	54.3	455	1278	139.2	8.67	2.68
SSW	Artificial Record	–	–	0.5	255.2	541	13,584	376.1	40.46	21.92

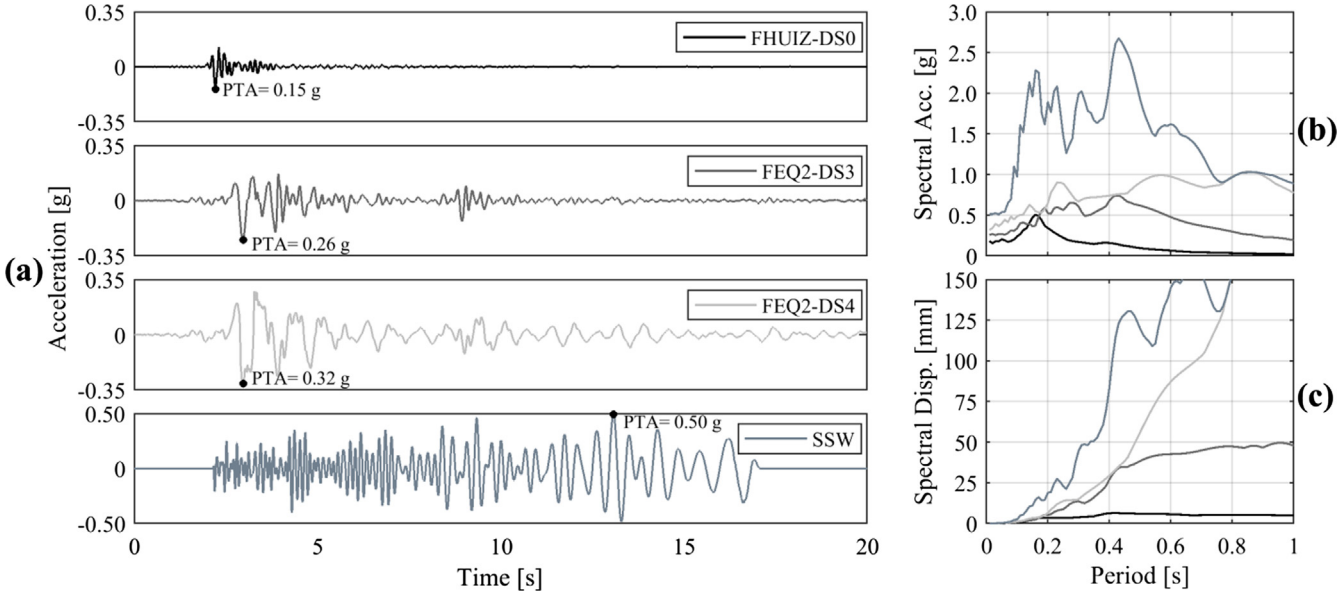

Fig. 6. Acceleration time histories of the employed table motions (a) 5% damped acceleration (b) and displacement (c) response spectra.

0.5 s) are listed in Table 3. Fig. 6 illustrates their 100% scaled acceleration time histories along with associated acceleration and displacement (5% damped) spectra.

The sequence of input motions each specimen was subjected to along with respective scaling factors (linear scaling with respect to *PTA*), measured *PTA* and maximum wall displacements are summarised in Table 4. For the first specimen (CS-010/005-RR), the reported displacement is measured at mid-height of the specimen (*MHD*-Mid height displacement) while for all other specimens this value is recorded at the top (*TD*-Top displacement). It should be noted that the part of the testing sequence when an overburden pressure of 0.10 MPa was maintained on the OOP panel has been highlighted in grey. The experiment after which first cracking was observed by visual inspection has been marked in bold for every specimen. No cracking prior to collapse was observed for the fifth specimen (CAV-000-RF). In general, after observations of damage which could potentially compromise the stability of the OOP panel, incremental testing was resumed again from a lower value of *PTA*.

4. Test results

This section discusses the results of the tests: examining the wall dynamic properties and their evolution, the observed damage patterns, failure mechanisms and hysteretic behaviour. Before discussing in detail the aforementioned aspects, it is worth noticing that the condition of each specimen at the end of each test was classified according to the definition of the following five damage states:

- DS1: no visible structural damage;
- DS2: slight structural damage;
- DS3: moderate damage with the full development of crack pattern corresponding to collapse mechanism;
- DS4: heavy damage with negligible residual capacity of resisting horizontal and vertical loads;
- DS5: very heavy damage with partial or global collapse of the panel.

Fig. 7 shows qualitatively these different damage states. It is to be noted that the nature of dynamic testing did not allow a test-by-test stable transition between one damage state and the next one. Very often the specimens experienced more than one damage states during a single test (e.g. CAV-000-RF during just Test #21 transitioned from DS1 to DS5).

4.1. Dynamic identification

As already mentioned in Section 3.3, low amplitude random excitations (RN) were used in between test runs to identify the dynamic properties of the specimens. These tests were conducted in the testing sequence corresponding to transitions between FEQ2-DS3 and FEQ2-DS4 or when structural distress was observed. Particular interest was given especially to the frequency and time period associated with the first natural mode of vibration of the specimens. Frequency domain decomposition was implemented in order to identify these natural frequencies [42]. The first natural mode of vibration of the specimens was observed to be dependent highly on the boundary conditions adopted. All specimens that had their top edge free: a wall with an opening, walls in CS and clay masonry and the cavity wall exhibited a first mode of vibration around 0.075 s (13.3 Hz) compared to 0.044 s (22.7 Hz) for the specimen with its top edge fixed in their undamaged configurations. These periods are in agreement with linear elastic eigenvalue

Table 4
Testing sequence of all specimens.

	CS-010-RR		CS-005-RR		CS-000-RF				CSW-000-RF				CL-000-RF				CAV-000-RF			
T#	Test Input	S.F.	*PTA* [g]	*MHD* [mm]	Test Input	S.F.	*PTA* [g]	*TD* [mm]	Test Input	S.F.	*PTA* [g]	*TD* [mm]	Test Input	S.F.	*PTA* [g]	*TD* [mm]	Test Input	S.F.	*PTA* [g]	*TD* [mm]
1	RN	100%	+0.06	-	RN	100%	-0.04	-	RN	100%	+0.05	-	RN	100%	-0.07	-	RN	100%	-0.06	-
2	FHUIZ-DS0	50%	-0.07	+0.1	FHUIZ-DS0	50%	-0.07	+0.2	RN	100%	+0.06	-	FHUIZ-DS0	50%	-0.074	-0.3	FHUIZ-DS0	50%	-0.07	-0.3
3	FHUIZ-DS0	100%	-0.16	+0.2	FHUIZ-DS0	100%	-0.15	+0.5	FHUIZ-DS0	50%	-0.07	-0.3	FHUIZ-DS0	100%	-0.16	+0.5	FHUIZ-DS0	100%	-0.16	+0.5
4	FHUIZ-DS0	150%	-0.20	+0.3	FHUIZ-DS0	150%	-0.23	+0.7	FHUIZ-DS0	100%	-0.16	+0.5	FHUIZ-DS0	150%	-0.19	+0.6	FHUIZ-DS0	150%	-0.23	+0.7
5	FEQ2-DS3	40%	-0.11	+0.1	RN	100%	+0.08	-	FHUIZ-DS0	150%	-0.22	+0.7	FEQ2-DS3	50%	-0.13	+0.5	FEQ2-DS3	50%	-0.13	+0.6
6	FEQ2-DS3	89%	-0.22	+0.1	FEQ2-DS3	50%	-0.16	+0.4	FEQ2-DS3	50%	-0.13	+0.5	FEQ2-DS3	89%	-0.23	+0.8	FEQ2-DS3	89%	-0.26	+1.0
7	FEQ2-DS3	100%	-0.27	+0.2	FEQ2-DS3	89%	-0.23	+0.6	FEQ2-DS3	89%	-0.25	+0.9	FEQ2-DS3	100%	-0.28	+0.9	FEQ2-DS3	100%	-0.27	+1.1
8	FEQ2-DS3	125%	-0.31	+0.2	FEQ2-DS3	100%	-0.25	+0.7	FEQ2-DS3	100%	-0.27	+1.0	FEQ2-DS3	125%	-0.31	+1.1	FEQ2-DS3	125%	-0.32	+1.4
9	RN	100%	+0.07	-	FEQ2-DS3	125%	-0.34	+0.9	FEQ2-DS3	125%	-0.31	+1.2	RN	100%	-0.06	-	RN	100%	+0.06	-
10	RWA	100%	+0.30	-0.2	FEQ2-DS4	100%	-0.39	+1.0	RN	100%	+0.05	-	FEQ2-DS4	50%	-0.16	-0.8	FEQ2-DS4	50%	-0.16	-0.9
11	FEQ2-DS4	50%	-0.17	-0.1	FEQ2-DS4	125%	-0.38	-1.3	FEQ2-DS4	50%	-0.16	-0.8	FEQ2-DS4	100%	-0.32	-1.3	FEQ2-DS4	100%	-0.34	-1.5
12	FEQ2-DS4	100%	-0.32	-0.2	FEQ2-DS4	150%	-0.46	-1.6	FEQ2-DS4	100%	-0.30	-1.4	FEQ2-DS4	125%	-0.39	-1.6	FEQ2-DS4	125%	-0.39	-1.8
13	FEQ2-DS4	125%	-0.38	-0.3	FEQ2-DS4	175%	-0.54	-2.0	FEQ2-DS4	125%	-0.39	-1.7	FEQ2-DS4	150%	-0.48	-1.9	FEQ2-DS4	150%	-0.48	-2.0
14	FEQ2-DS4	150%	-0.47	-0.3	FEQ2-DS4	200%	-0.68	-2.4	FEQ2-DS4	150%	-0.45	-2.0	FEQ2-DS4	175%	-0.53	-2.1	FEQ2-DS4	175%	-0.57	-2.4
15	FEQ2-DS4	200%	-0.74	-0.4	FEQ2-DS4	250%	-0.78	-3.0	FEQ2-DS4	175%	-0.53	-2.3	FEQ2-DS4	200%	-0.67	-2.5	FEQ2-DS4	200%	-0.63	-2.4
16	FEQ2-DS4	250%	-0.91	+0.6	FEQ2-DS4	300%	-0.95	-3.4	FEQ2-DS4	200%	-0.65	+2.6	FEQ2-DS4	250%	-0.76	+2.7	RN	100%	-0.09	-
17	FEQ2-DS4	300%	-0.90	+0.6	FEQ2-DS4	350%	-1.10	+4.7	FEQ2-DS4	250%	-0.81	+3.0	FEQ2-DS4	300%	-0.94	+3.3	FEQ2-DS4	100%	-0.31	-1.6
18	FEQ2-DS4	100%	-0.32	-0.3	**FEQ2-DS4**	**400%**	**-1.28**	**+12.8**	FEQ2-DS4	300%	-0.91	-3.4	FEQ2-DS4	350%	-1.11	+5.0	FEQ2-DS4	250%	-0.86	+3.4
19	FEQ2-DS4	200%	-0.68	+0.5	RN	100%	+0.04	-	FEQ2-DS4	350%	-1.13	+4.1	RN	100%	-0.06	-	FEQ2-DS4	300%	-0.99	+3.9
20	FEQ2-DS4	300%	-1.05	+0.9	FHUIZ-DS0	100%	-0.15	+5.0	**FEQ2-DS4**	**400%**	**-1.28**	**+8.9**	FEQ2-DS4	100%	-0.30	-1.5	FEQ2-DS4	350%	-1.13	+4.8
21	FEQ2-DS4	400%	-1.18	+1.3	FEQ2-DS3	100%	-0.24	+4.9	RN	100%	-0.07	-	FEQ2-DS4	400%	-1.33	+8.5	**FEQ2-DS4**	**400%**	**-1.37**	**-113**
22	**FEQ2-DS4**	**600%**	**-1.93**	**+8.0**	**FEQ2-DS4**	**200%**	**-0.62**	**Coll.**	FHUIZ-DS0	100%	-0.15	+1.5	RN	100%	-0.07	-				
23	RN	100%	+0.08	-					FEQ2-DS3	100%	-0.25	-2.3	**FEQ2-DS4**	**500%**	**-1.71**	**Coll.**				
24	SSWx2	75%	+0.39	+3.0					FEQ2-DS4	100%	-0.33	+3.5								
25	SSWx2	200%	+0.99	+4.4					FEQ2-DS4	150%	-0.46	+5.1								
26	SSWx2	250%	+1.39	+9.0					FEQ2-DS4	200%	-0.78	-7.0								
27	RN	100%	-0.05	-					**FEQ2-DS4**	**300%**	**-0.91**	**+68**								
28	SSWx2	150%	+0.92	+7.2																
29	SSWx2	150%	+0.81	+5.4																
30	SSWx2	100%	+0.66	+5.5																
31	**SSW**	**300%**	**+1.42**	**Coll.**																

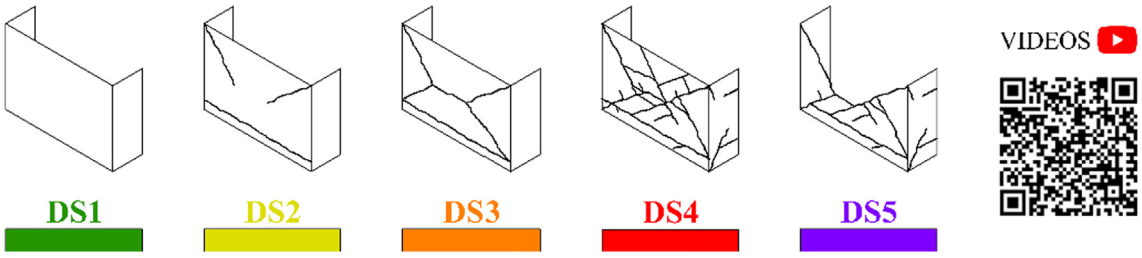

Fig. 7. Example scheme of crack pattern associated with different damage states and QR code to access YouTube playlist documenting the failure of each specimen [44].

analyses carried out for each of the walls using shell FE models constructed in SAP [43]. Distinct increases in the time period associated with the first natural mode of vibration could be observed in RN tests conducted after runs in which the specimen transitioned between the defined damage states (Table 5).

4.2. Damage patterns and failure mechanisms

The progression of damage in each specimen was quite complex. Nature and location of damage often changed with increasing seismic input as the incremental dynamic test progressed. Nevertheless, detailed condition mapping was carried out after each run in the incremental dynamic test sequence and all observed cracks are reported in this section along with the test in which they were observed. In tests where the wall collapsed onto the shake table, the cracks responsible allowing for the development of the failure mechanism were reproduced from videos of the test. Additionally, the observed failure mechanisms are compared with expected mechanisms reported in literature corresponding to different wall configurations (Fig. 8).

Table 5
Dynamic identification of the specimens.

CS-010/005-RR			CS-000-RF			CSW-000-RF			CL-000-RF			CAV-000-RF		
T# DSi	Freq. [Hz]	*T* [s]	T# DSi	Freq. [Hz]	*T* [s]	T# DSi	Freq. [Hz]	*T* [s]	T# DSi	Freq. [Hz]	*T* [s]	T# DSi	Freq. [Hz]	*T* [s]
1 DS1	22.9	0.044	1 DS1	13.7	0.073	1 DS1	13.5	0.074	1 DS1	12.8	0.078	1 DS1	12.6	0.079
9 DS1	22.9	0.044	5 DS1	13.4	0.074	2 DS1	12.8	0.078	9 DS1	12.6	0.080	9 DS1	12.3	0.082
23 DS2	17.0	0.059	19 DS3	6.8	0.148	10 DS1	12.6	0.080	19 DS2	12.4	0.081	16 DS1	12.1	0.083
27 DS2	17.0	0.059	–	–	–	21 DS2	9.9	0.101	22 DS2	11.6	0.087	–	–	–

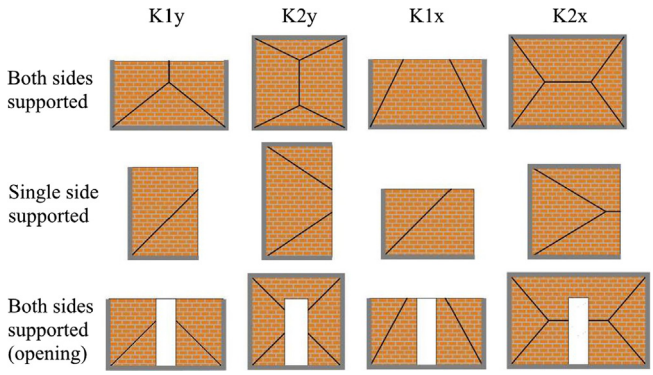

Fig. 8. Failure mechanisms reported in literature corresponding to various wall configurations [35].

To facilitate a better understanding of the failure modes of each wall, 3D deformed shapes were also constructed for critical tests. In each test, these shapes were produced at the instants in which the OOP panel had maximum displacement towards (positive) and away (negative) from the return walls. Such shapes (with a mesh of 50x50 elements along width and height of the panel) were constructed by performing linear interpolation for all points in the wall between locations where displacements were recorded and indicated by black spheres. The reported wall deflections were normalised with respect to the peak displacements occurring at that instant. Videos documenting the failure of each specimen can be viewed online [44].

4.2.1. Calcium silicate wall restrained at top and bottom extremities vertically loaded with 0.10 MPa and 0.05 MPa (CS-010-RR/CS-005-RR)

The first specimen in the CS-010-RR configuration remained in the elastic range (correspondingly to DS1) over the duration of its entire testing sequence. This corresponded to a *PTA* of 0.90 g and an associated peak *MHD* of 0.6 mm. Such a stiff response indicated that the specimen in this configuration was likely to fail at table accelerations unrealistic for low-rise URM buildings. Consequently, the vertical overburden on the OOP panel was reduced to 0.05 MPa. In this configuration, the specimen attained first cracking (DS2) during Test #22 (*PTA* = 1.93 g, peak *MHD* = 8.0 mm). First cracking consisted of two stepped diagonal cracks from the upper right and left corners, which met around the centre of the panel and continued down to a horizontal crack in the OOP panel and right return wall in the form of an almost completely straight-line crack (Fig. 9a). The deformed shape in the negative direction was seen to be very similar to what is expected for a slab fixed in both horizontal and vertical directions. In Test #26 (*PTA* = 1.39 g, peak *MHD* = 9.0 mm), a line crack appeared in the connection with the right return wall extending from the horizontal crack which appeared in Test #22. Additionally, an elongation of the pre-existing horizontal crack was observed in the left return wall (Fig. 9b). Despite the increase in observed structural distress, the specimen can be still considered to be in DS2 and this is also reflected by the fact that no change in dynamic properties of the specimen could be observed after this test (Table 5).

The specimen collapsed (DS5) transitioning through DS3/DS4 during Test #31 (*PTA* = 1.42 g). The cracks leading to the activation of the failure mechanism have been reproduced (in blue) from a careful examination of the video of the ultimate test (Fig. 9c). This mechanism is very similar to K2X (Fig. 8) with the exception of a horizontal crack that appeared in the mid height of the right part of the wall (Fig. 9f). The appearance of this crack can be attributed to the premature failure of the connection with the right return wall in Test #26. In fact, the deformed shape constructed for Test #28 in the negative direction very clearly exhibits what can be considered very similar to a one-sided one-way rocking motion in the right part of the specimen (Fig. 9g). Although the additional cracks observed during Test #31 (Fig. 9c) could not be seen during Test #28, this deformed shape (Fig. 9e) is highly indicative of the failure mechanism observed and DS3 being reached. It can be observed from all the deformed shapes that the part of the OOP panel below the horizontal crack occurring in Test #22 remained relatively immobilized.

4.2.2. Calcium silicate wall free on top (CS-000-RF)

Damage pattern and failure mechanisms observed for the CS-000-RF specimen were slightly different from K1Y (Fig. 8). The wall

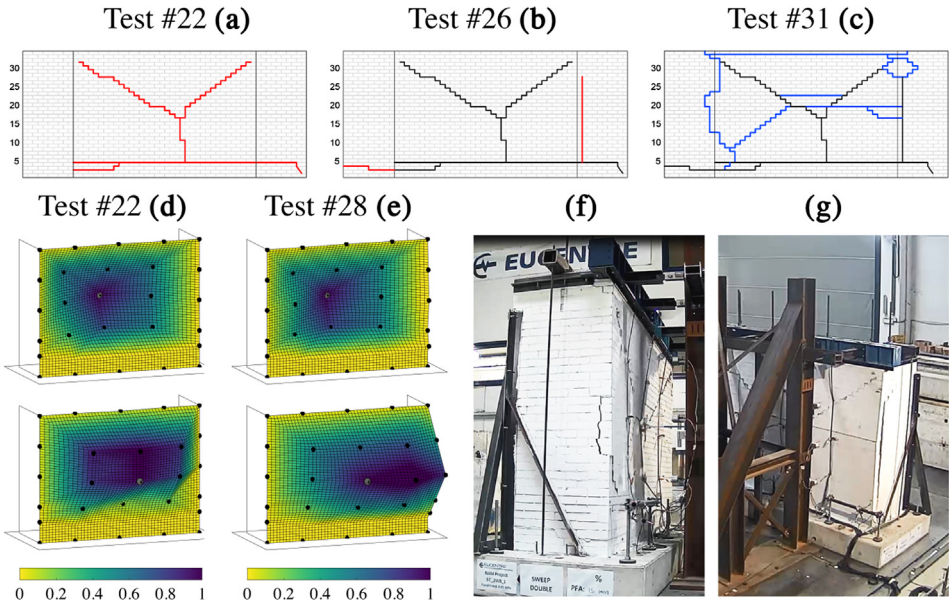

Fig. 9. CS-005-RR: evolution of the crack pattern (a–c). 3D deformed shapes in positive (top) and negative (bottom) directions: first cracking (Test #22, *PTA* = 1.93 g, Peak *MHD* = +8.0 mm/−2.4 mm) (d) and failure mechanism (Test #28, *PTA* = 0.92 g, Peak *MHD* = +7.2 mm/−2.9 mm) (e); pictures of specimen collapse (f and g).

reached first cracking condition associated with a complete development of a mechanism of the left portion of the OOP panel (DS3) during Test #18 (*PTA* = 1.28 g, peak *TD* = 12.8 mm). Two vertical line cracks appeared at the connection of the left return wall and at the centre of the OOP panel. A smaller vertical line crack was also seen near the connection with the right return wall. Horizontal and stepped diagonal cracks could also be observed in the lower part of the OOP panel (Fig. 10a). Deformed shapes during this test were very similar in both the positive and negative directions with highest displacements observed along the central line crack (Fig. 10c).

The specimen reached collapse (DS5) during Test #22 (*PTA* = 0.62 g). The cracks that led to the development of DS3 during this test have also been carefully reproduced from a video of the test. Full development of line cracks along the connections with both the return wall was observed (Fig. 10b). This led to the collapse of the specimen by overturning of the part of the OOP panel above the horizontal crack together with rotation of the right and left panels about their connections with the return walls (Fig. 10e and f). Since only limited instruments were acquiring data at this level of high seismic input, the deformed shape in Fig. 10d does not correspond to recorded experimental data and was produced to give only a better visual representation of the failure mechanism.

4.2.3. Calcium silicate wall with opening and free on top (CSW-000-RF)

Damage pattern and failure mechanisms observed for the CSW-000-RF specimen were quite different from expected mechanisms for similar wall configurations reported in literature. DS2 was realised under significant seismic input occurred during Test #20 (*PTA* = 1.28 g, peak *TD* = 8.9 mm). Observed damage consisted of a vertical line crack at the connection with the left return wall and a stepped crack extending from the upper left corner of the window to the top of the specimen. The initiation of a horizontal crack along the bed joint from the lower left corner of the window was also observed (Fig. 11a). Both deformed shapes in positive and negative directions show the rotation of the longer part of the OOP panel and the part on top of the window (Fig. 11c). The part of the specimen below the opening showed relatively less deformation.

The specimen underwent very extensive damage (DS4) during Test #27 (*PTA* = 0.91 g, peak *TD* = 68 mm). Since DS5 was not attained, the crack pattern reported was produced by visual examination after the experiment was over (Fig. 11b). Despite the extensive cracking surveyed at the end of the test, the mechanism was triggered by the horizontal crack around the mid-height of the panel on the left of the opening and the diagonal crack propagating towards the left return wall. The resulting deformed shapes (almost symmetric in both directions) are indicative of the failure mechanism showing a localisation of the deformation in the portion of the specimen above these cracks (Fig. 11d). These shapes are well indicative of the complexity that was involved in the failure mechanism. Rotation of the multiple panels into which the wall was divided can be clearly observed from the residual deformation at the end of the test (Fig. 11e).

4.2.4. Clay wall free on top (CL-000-RF)

Damage pattern and failure mechanisms observed for the CL-000-RF specimen were very similar to K1Y (Fig. 8). DS2 of the specimen occurred during Test #18 (*PTA* = 1.11 g, peak *TD* = 5.0 mm). A horizontal crack in the 3rd bed joint from the bottom throughout the OOP panel could be observed.

Additionally, initiation of some stepped diagonal cracks could be seen in the left return wall and corner of the OOP panel above this horizontal crack (Fig. 12a). The collapse (DS5) of this specimen was reached during Test #23 (*PTA* = 1.71 g). Although the ultimate test led to collapse and extensive cracking, careful examination of the video of the test revealed that the complete development of the failure mechanism (DS3) also occurred in the same test by the formation of two stepped diagonal cracks starting from the two lower corners of the OOP panel above the horizontal crack. These two diagonal cracks meet near the centre of the OOP panel and propagate to the top of the specimen in the form of another stepped crack (Fig. 12b and f). The analysis of the specimen deformation shows the evolution of the deflected shape from an almost fixed-fixed horizontally spanning beam (Test #21, Fig. 12d) towards a concentration of displacement along the central crack (Test #23, Fig. 12e). This latter deformed shape was constructed at a

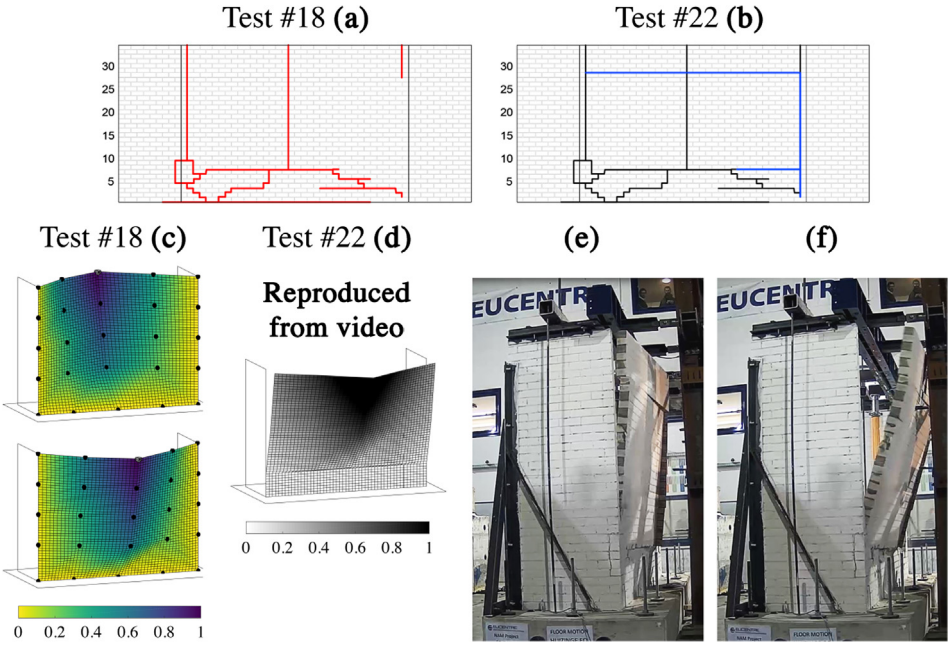

Fig. 10. CS-000-RF: evolution of the crack pattern (a and b). 3D deformed shapes in positive (top) and negative (bottom) directions: first cracking (Test #18, *PTA* = 1.28 g, Peak *TD* = +12.8 mm/−8.4 mm) (c) and failure mechanism (reproduced from video); pictures of OOP panel overturning (e and f).

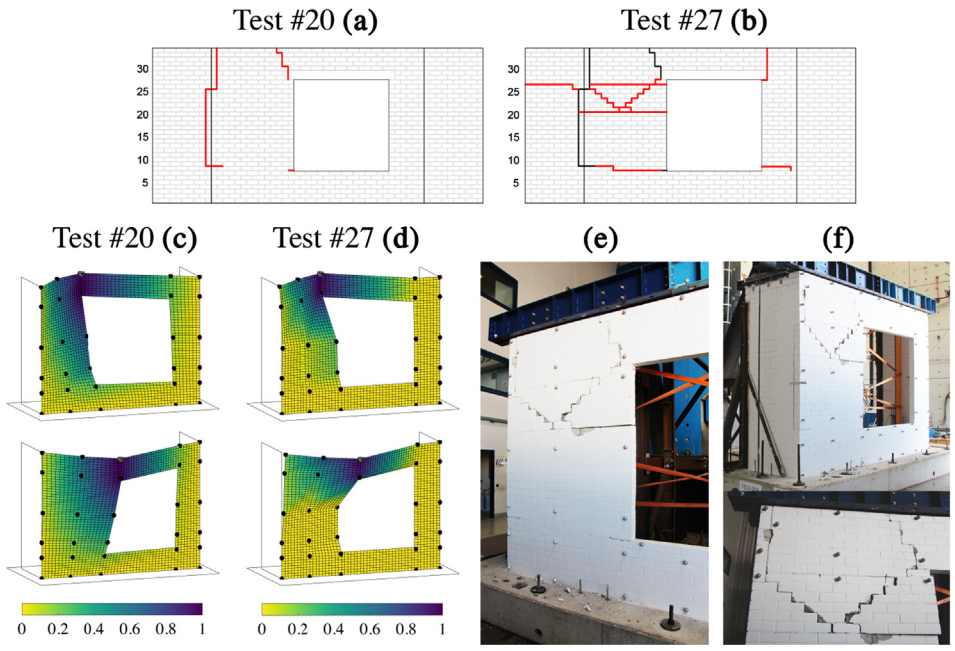

Fig. 11. CSW-000-RF: evolution of the crack pattern (a and b). 3D deformed shapes in positive (top) and negative (bottom) directions: first cracking (Test #20, *PTA* = 1.28 g, Peak *MHD* = +8.9 mm/−7.3 mm) (c) and failure mechanism (Test #27, *PTA* = 0.91 g, Peak *TD* = +68.3 mm/−55.3 mm) (d); pictures of the residual deformation at the end of the test (e and f).

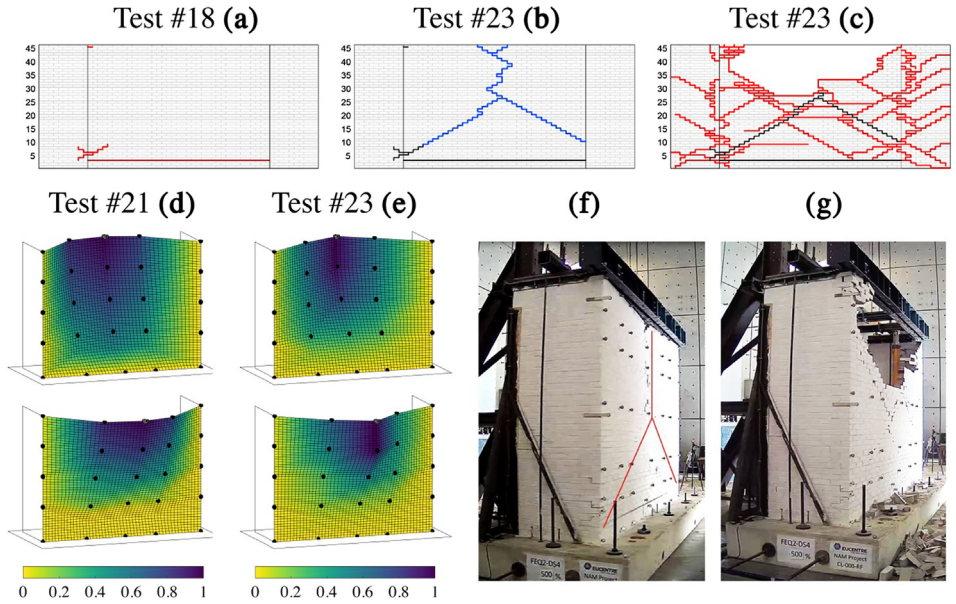

Fig. 12. CL-000-RF: evolution of the crack pattern (a–c). 3D deformed shapes in positive (top) and negative (bottom) directions: first cracking (Test #21, *PTA* = 1.33 g, Peak *TD* = +8.5 mm/−5.4 mm) (d) and failure mechanism (Test #23, *PTA* = 0.91 g, Peak *TD* = +113.9 mm/−172.0 mm) (e); pictures of the residual deformation at the end of the test (f and g).

particular instant of the ultimate test before the specimen collapse when it was clearly representative of the failure mechanism. Fig. 12c and g represents the collapsed state of the specimen at the end of the testing sequence.

4.2.5. Cavity wall (CS-Clay) with both leaves free on top (CAV-000-RF)

Similar to previous experiments [7], the adopted L-shaped ties despite having negligible flexural stiffness ensured a sufficient coupling of the horizontal displacement of the two leaves (*i.e.* limiting the differential displacement and maintaining the gap) up to collapse. This was due to the axial stiffness and bond of the ties as well as the slenderness of the two leaves. Damage pattern and failure mechanisms observed for the clay leaf of CAV-000-RF specimen were very similar to K1Y. Both clay and CS leaves exhibited failure mechanism consistent with the ones observed for CL-000-RF and CS-000-RF, respectively. Unlike all other specimens, no cracking was observed for any of the two leaves composing the cavity wall until the ultimate test. The specimen reached extensive damage condition (DS4) directly in Test #21 (*PTA* = 1.37 g). Also in this case, DS5 was not attained and the crack patterns reported

were produced by visual examination at the end of the test sequence. Cracks in the CS leaf included line cracks at the centre of the OOP panel and at the connection with the return walls (with significant residual displacement at the end of the test). A horizontal crack was detected at the first bed joint from the bottom. Another horizontal crack was observed at the mid-height of this leaf corresponding to the location of the ties (Fig. 13a).

The deformed shape in the positive direction shows the rotation of the two panels individuated by the central line crack as well as sliding of the wall on the horizontal crack (Fig. 13c). Since this sliding was not directly measured, it was reproduced from a critical assessment of the video. Because of this sliding, a residual displacement of approximately 40 mm (in the positive direction) could be observed in the inner CS leaf at the end of Test #21. The outer clay leaf showed extensive diagonal cracking at the end of the ultimate test (Fig. 13b). The deformed shapes in both positive and negative directions, however, confirm the activation of the K1Y mechanism (Fig. 13d). All deformed shapes were constructed at a particular instant of the ultimate test when they were clearly representative of the failure mechanism (DS3).

4.3. Hysteretic behaviour

The evolution of the hysteretic response of each specimen is illustrated in Figs. 14 and 15. In order to facilitate the comparison between all the specimens, these responses have been computed in terms of shear coefficient (*SC*) vs. *MHD* (mid-height displacement) for CS-000-RR and *SC* vs. *TD* (top displacement) for all other specimens. The *SC* was calculated from the walls' inertial force (V_w) as follow:

$$SC = \frac{V_w}{m \cdot g} \tag{2}$$

where m is the mass of the OOP panel of each specimen (Table 1) and g is the acceleration due to gravity. Time-histories of inertial forces associated with the OOP panel were computed by multiplying the acceleration recorded by accelerometers with a tributary mass assigned to them. The mass of the OOP panel was assumed to be lumped at the accelerometer locations. Tributary mass assigned to each accelerometer were modified throughout the testing sequence based on the progression of damage and crack pattern. The evolution of the masses assigned to each accelerometer for every specimen can also be downloaded from www.eucentre.it/nam-project.

The hysteretic response of each specimen has been divided into three phases superimposed on each other with different colours: pre-cracking, first cracking and post-cracking tests. The pre-cracking phase corresponds to tests in which the specimens remained in DS1. It is to be noted that peak strength in term of forces was often realised before the failure mechanism was fully activated *i.e.* attainment of DS3. As an example, for CS-000-RF and making reference to Table 4, Test #1–17 are included in the pre-cracking, Test #18 in the first cracking and Test #19–22 in the post-cracking phases respectively. The inertial force values associated with the peak *SC* and corresponding displacements, in both positive and negative cycles are provided in the legend of each hysteretic response. The peak response displacement and associated inertial force before the loss of equilibrium are also reported for specimens tested up to DS5. These values have been provided for CS-005-RR, CS-000-RF and CL-000-RF but may be not visible from the force-displacement response because they are beyond the scale of the axes of Fig. 14 (to allow a better appreciation of the shape of small-displacements hysteretic loops). It is to be noted that the *TD* plotted in the hysteretic response of CAV-000-RF is measured on top of the CS leaf.

All specimens exhibited a rather brittle response. This holds particularly for the CS specimens where the cracking was controlled by line failure (*i.e.* the flexural tensile strength of units). Peak inertial force that was sustained by specimens CS-005-RR, CS-000-RF and CSW-000-RF corresponded to very low (less than 6 mm) values of *MHD* and *TD* respectively. Strength and stiffness degradation took place quite quickly over a few response cycles and very limited range of displacement. This is also

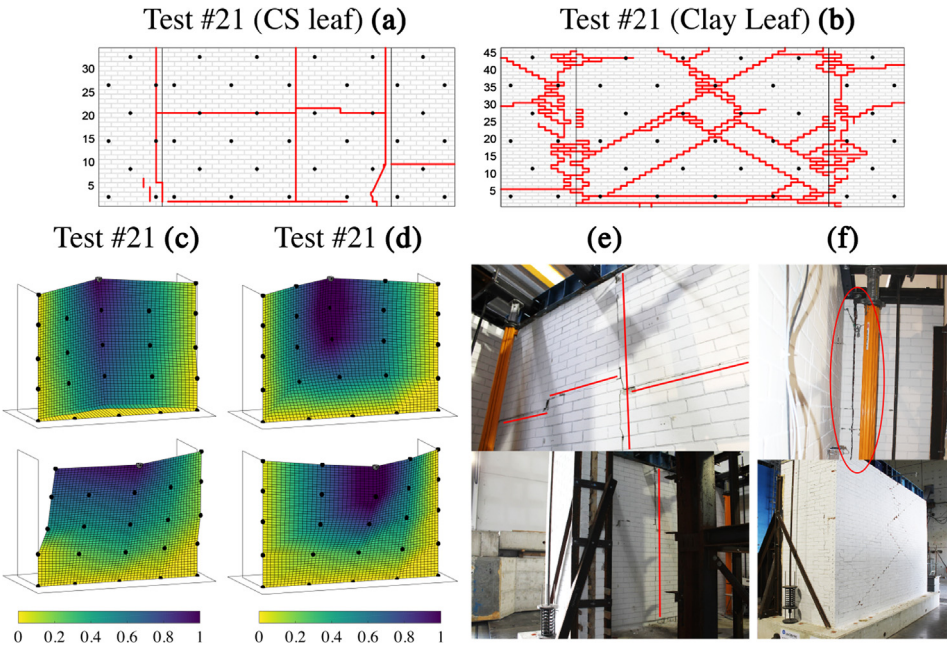

Fig. 13. CAV-000-RF: crack pattern (a and b). 3D deformed shapes in positive (top) and negative (bottom) directions: CS inner leaf (Test #21, *PTA* = 1.37 g, Peak *TD* = +40.4 mm/−25.0 mm) (c) and clay outer leaf (Peak *TD* = +35.8 mm/−25.4 mm) (d); pictures of residual deformation on CS inner leaf (e), failure of CS left return wall connection (f, top), clay leaf damage (f, bottom).

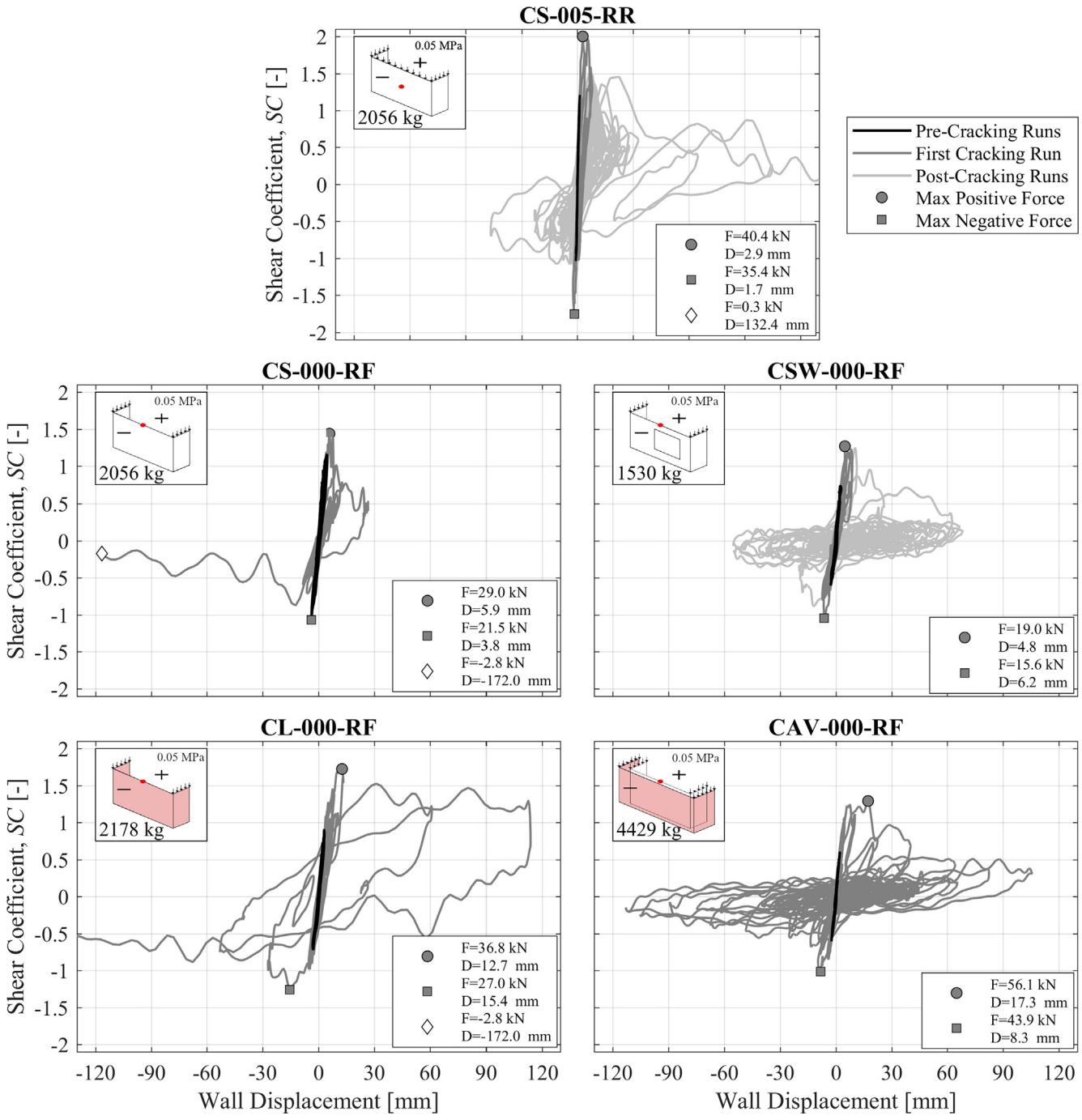

Fig. 14. Hysteretic response of every specimen (location of displacement indicated by red dot; circular and rectangular markers identify attainment of peak forces in positive and negative directions respectively; diamond marker indicates force and displacement at the location where recording has been terminated for specimens tested up to DS5). (For interpretation of the references to colour in this figure legend, the reader is referred to the web version of this article.)

reflected by the number of tests in the testing sequence between DS2 being reached and the ultimate test for these specimens (Table 4).

The *MHD* associated with peak inertial strength for CS-005-RR, attained during the Test #22 when first cracking was observed, was relatively lower compared to the other specimens (less than 3 mm). The wall was also able to sustain a large number of tests adopting a very demanding signal (SSW) post-cracking. This is due to the combined effect of the top horizontal restraint and the higher acting axial load. The failure mechanism completely developed only at *MHD* of 15 mm, with stiffness and strength degradation taking place within this range of displacement (3–15 mm). Beyond this limit, the wall lateral resistance relied only on the combination of rocking and friction (coming from the frictional torsional resistance of bed-joints). Although associated with higher energy dissipation, the shape of the resulting force-displacement loops is very similar to the ones observed in one-way bending behaviour of vertically spanning walls.

Regarding CL-000-RF, the peak inertial force was attained at higher level of *TD* (12.7 mm) compared to all other specimens. Post-peak response cycles (associated with stiffness degradation) showed the capability of resisting significant values of lateral load

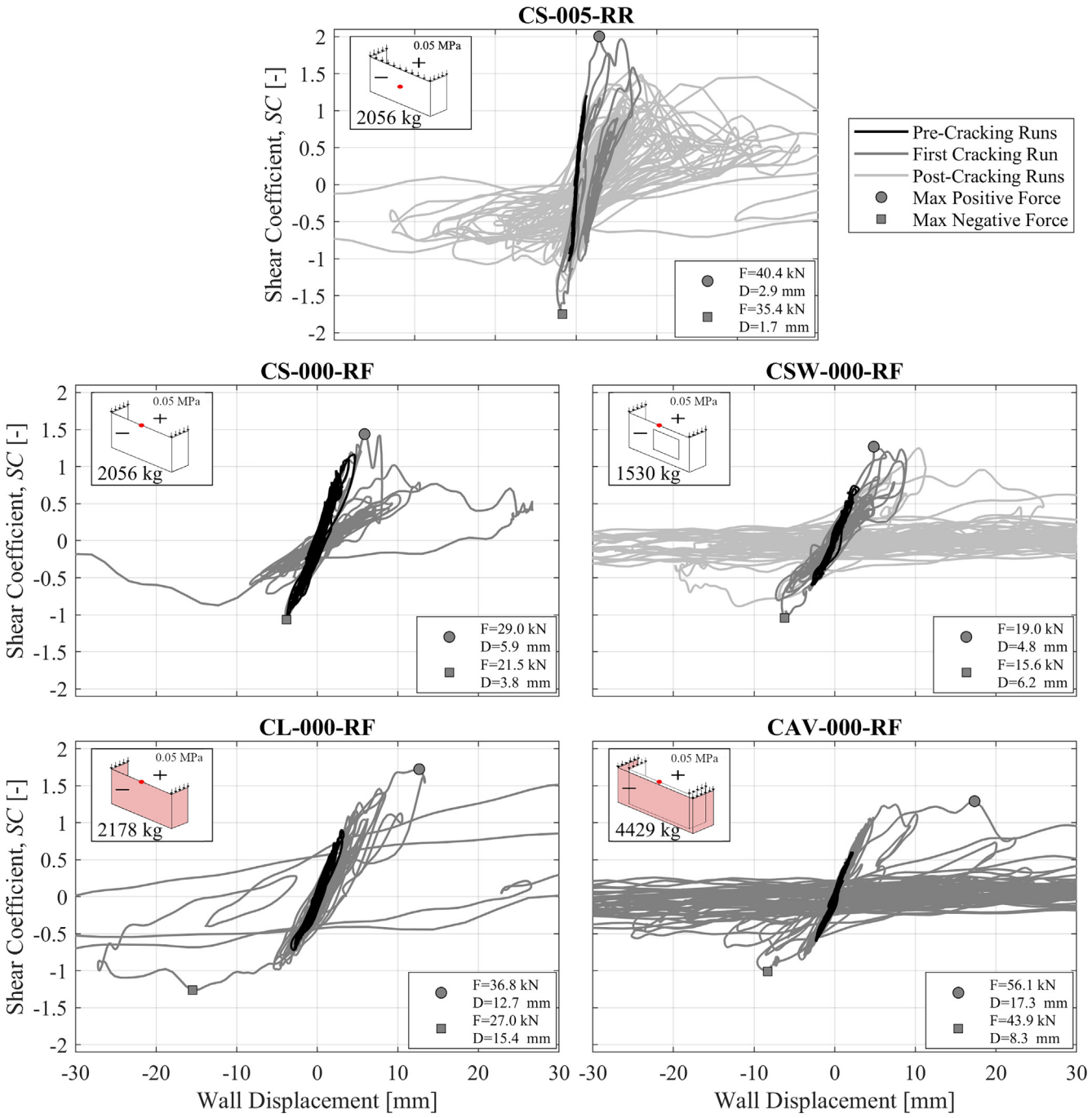

Fig. 15. Close-up of the hysteretic response of every specimen (location of displacement indicated by red dot, circular and rectangular markers identify attainment of peak forces in positive and negative directions respectively). (For interpretation of the references to colour in this figure legend, the reader is referred to the web version of this article.)

up to *TD* of 100 mm and also higher energy dissipation. This is in accordance with observed extensive stepped cracking where the energy dissipation is mainly controlled by the torsional friction response.

CS-000-RF exhibited a particularly brittle response. At the attainment of peak inertial force associated with a *TD* of 5.9 mm, the failure mechanism had almost completely developed. Given the predominant occurrence of line cracking, the very limited post peak capacity was primarily controlled by rocking.

CSW-000-RF was able to sustain peak inertial force up to *TD* of approximately 10 mm. At higher displacements, significant stiffness and strength reduction was observed with limited residual lateral capacity mainly coming from the torsional friction resistance of bed-joints.

The hysteretic response exhibited by the CAV-000-RF was very similar to CL-000-RF. Also in both specimens, significant cracking occurred only in the ultimate test. Peak inertial force was attained at a *TD* of 17.3 mm and quick strength and stiffness degradation were observed after attainment of peak strength.

Due to the nature of the testing performed it was not possible to quantify an exact ultimate displacement associated with each specimen.

The observed hysteretic behaviour of CS panels appears to be quite different from the results of two-way bending OOP cyclic and monotonic airbag testing carried out by Griffith and Vaculik and Griffith et al. [45,15] and Messali et al. [16] on clay and CS specimens respectively. Although the displacements at which peak strengths were attained are quite similar, the capability of sustaining large inertial forces over a wide range of displacement (around 30 mm) was not observed. Moreover, the lateral load capacity at displacements equal to half of the wall thickness for CS walls was in all the cases lower than 0.3 times the peak capacity. However, the envelope lateral load capacity of CL-000-RF and CAV-000-RF at the same displacement level were considerably higher (0.6 and 0.4 respectively).

4.4. Specimen strength capacity

Specimen capacities were plotted in terms of *PTA* sustained by the walls vs. peak *MHD* or *TD* exhibited in the corresponding test (Fig. 16). These values were plotted only for the tests in which the employed signal was FEQ2-DS4 and SSW. *PTA* values corresponding to the ultimate test are provided even if the associated displacement is not known for tests in which the specimen collapsed onto the shake table. In case of CSW-000-RF and CAV-000-RF, associated peak response displacement recorded before the loss of equilibrium occurred are mentioned. The curves are not extended until that point in order to appreciate the initial and changes in stiffness associated with the specimens. The change in applied overburden pressure for the first specimen (from CS-010-RR to CS-005-RR configuration) did not affect the specimen initial stiffness too much. CS-010-RR/CS-005-RR was much stiffer compared to all other specimens which presented a very similar initial stiffness. This is in agreement with results of dynamic identification (Table 5).

In case of CS-005-RR, distinct changes in stiffness coincided with Test #18 and #26 which corresponded to tests in which first cracking and consequent damage at the connection with the right return wall respectively were observed. Similar behaviour is also noticed for CSW-000-RF. The low post cracking residual strength capacity associated with CS-000-RF resulted in it collapsing very soon after cracking. Cracking and collapse coincided for CL-000-RF and CAV-000-RF but at a higher *PTA* with respect to the other specimens under same boundary conditions.

5. Analysis and interpretation of the wall's experimental behaviour

In this section, a critical interpretation of the exhibited experimental behaviour in terms of force capacity (peak strength) is attempted. Initially, state-of-art codified models based on the principle of virtual work present currently in literature and their governing theoretical formulation are presented. Their effectiveness in predicting the wall peak strengths is then reviewed. Consequently, the principles of virtual work are explicitly applied to observed failure mechanisms in the experimental campaign in an attempt to understand their response.

5.1. State-of-art analytical models

Current analytical formulations for studying the OOP response of URM masonry are based on the principle of virtual work (VW). Strength associated with a wall is calculated by considering that all the work done by applied external loads gets converted into strain energy associated with wall deformation. In particular, external loads are assumed to be acting in the form of a uniformly applied pressure ($w(x,y) = w$) on the wall face area where x and y are axes perpendicular to each other along the wall face as proposed by Griffith and Vaculik [45]. The external work (E'_{tot}) is then calculated by integrating the product of this applied pressure and the virtual displacement ($u'(x,y)$) of the wall:

$$E'_{tot} = \int_Y \int_X w(x,y)u'(x,y)dxdy = wV'_{tot} \tag{3}$$

where V'_{tot} is the total displaced volume calculated as $V'_{tot} = \int_Y \int_X u'(x,y)dxdy$. The total internal energy (U'_{tot}) is computed as the sum of strain energies associated with all occurring cracks as product of crack moments (M) along with their associated crack rotations (θ)

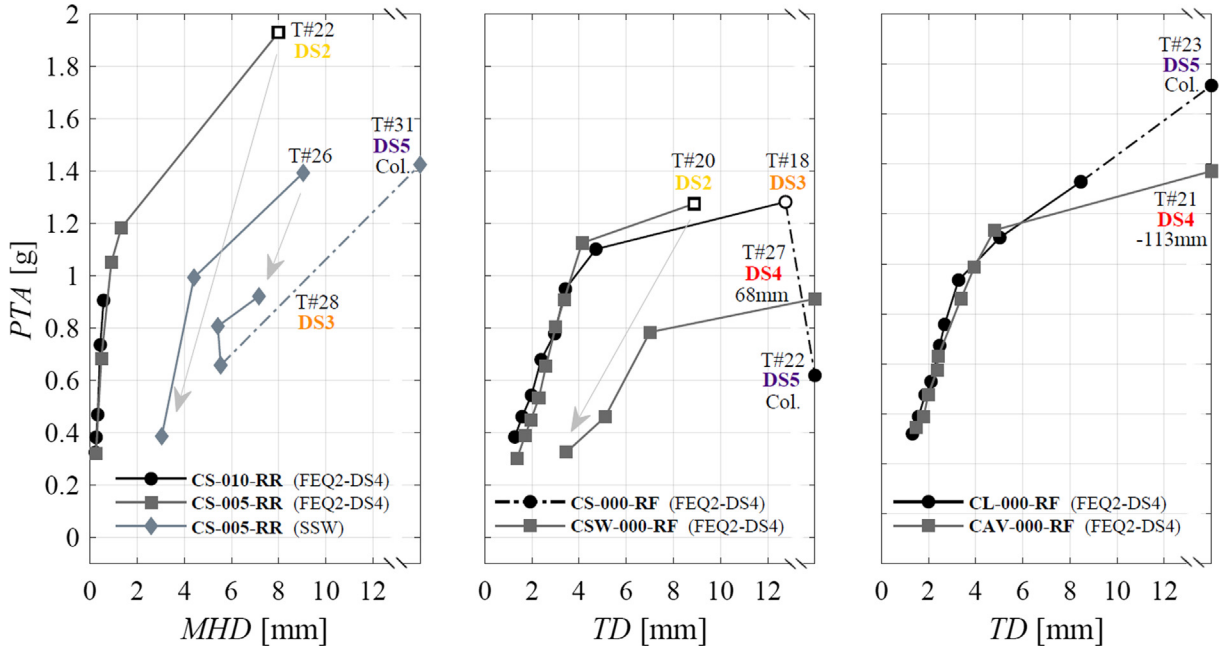

Fig. 16. Specimens capacities in terms of *PTA* vs. Wall Displacement.

(i is the crack index of individual cracks and n is the total number of cracks):

$$U'_{tot} = \sum_{i=1}^{n} M_i \delta\theta_i \tag{4}$$

Equating external and internal work (Eqs. (3) and (4)), the strength associated with a specimen (w) is calculated as a function of crack moments (M) and geometry of the failure mechanism (θ, V'_{tot}):

$$w = \frac{U'_{tot}}{V'_{tot}} = \frac{\sum_{i=1}^{n} M_i \delta\theta_i}{V'_{tot}} \tag{5}$$

For OOP response of URM walls, the virtual work method has already been codified [46] and also implemented in the Australian Masonry Structures Code, AS 3700 [47]. However, moment capacities associated with cracks in AS 3700 are calculated using empirical and dimensionally inconsistent formulation. A more rational mechanical model to calculate these capacities were developed by Willis [48] and successively revised by Griffith and Vaculik [45], which are presented here. Moment capacity due to horizontal bending M_h (per unit crack length) is calculated as the minimum of the values associated with line or stepped cracks:

$$M_h = lesser\ of \begin{cases} \frac{1}{2(h_u+t_j)}\left[(f_{ut} - \nu\cdot\sigma)\cdot h_u \frac{t_u^2}{6}\right] & (line\ failure) \\ \frac{1}{h_u+t_j}\left[\tau_u \cdot k_b \cdot 0.5 \cdot (l_u + t_j)\cdot t_u^2\right] & (stepped\ failure) \end{cases} \tag{6}$$

Moment capacity associated with diagonal bending M_d (per unit crack length) is calculated as:

$$M_d = \frac{\sin\varphi}{h_u + t_j}\left[(\sin\varphi)^3 \cdot \tau_u \cdot k_b \cdot 0.5 \cdot (l_u + t_j)\cdot t_u^2 + (\cos\varphi)^3 \cdot (f_{mt} + \sigma)\cdot \frac{0.5\cdot(l_u + t_j)\cdot t_u^2}{6}\right] \tag{7}$$

In Eqs. (6) and (7) l_u, h_u and t_u are the length, height and thickness of a brick unit; t_j is the thickness of a mortar joint; φ is the assumed global slope of a stepped diagonal crack calculated from unit geometry as $2(h_u + t_j)/(l_u + t_j)$ (36.12 and 28.83 degrees for CS and clay masonry of this paper, respectively) implying that diagonal stepped cracks follow the natural slope dictated by the size of units and their bond (overlap); f_{mt} is the flexural tensile strength of masonry as a composite; f_{ut} the flexural tensile strength of a brick unit, σ is the vertical pre-compression at mid height of the wall and ν is the Poisson's ratio of masonry which was taken as 0.2 here. τ_u here denotes the ultimate torsional shear stress in a masonry bed joint which was proposed by Willis to be calculated as $\tau_u = 0.9\sigma + 1.6 f_{mt}$ while k_b is the same numerical factor used while performing torsional shear testing to compute shear stress due to torsion acting on a rectangular shaft, adopted as 0.213 [36]. Significant disparity was observed in the ultimate shear stress of a bed-joint calculated using this equation and that obtained from torsional shear testing of masonry reported in Section 2.3. Calculations were also performed considering τ_u [MPa] = 1.14σ + 1.81 and τ_u [MPa] = 1.55σ + 1.07 for CS and clay masonry respectively. Table 6 summarises the values of moment capacities (per unit crack length) obtained with Eqs. (6) and (7) considering relationships for ultimate shear stress in a bed joint as proposed by Willis [48] and also experimentally derived (values of moment capacities provided in bold refer to the value that was used in the calculations *i.e.* the critical among stepped and line failure for horizontal bending capacity, for diagonal bending capacity only one value was calculated and hence used). It is to be noted that these assumptions in terms of the ultimate shear stress value affect only the horizontal moment capacity when it is governed by stepped failure and the diagonal moment capacity. Both moment capacities result to be higher in the case of the assumption of experimentally derived τ_u. In agreement with the observed experimental response, for CS specimens the lesser horizontal moment capacity is the one provided by line failure criteria. For clay specimens, still in agreement with experimental observations, the failure mechanism in horizontal bending is instead governed by stepped failure for both values of τ_u assumed.

Important assumptions inherent in all forms of analytical methods used in this paper are: moment capacities of all diagonal and horizontal cracks are reached simultaneously and the resistance provided by horizontal cracks to peak strength is neglected [48,45].

5.2. Predictions of peak strength

The methods codified in the AS 3700 (SC_{AS}, w_{AS}) and proposed by Griffith and Vaculik [45] (SC_{GV}, w_{GV}) were applied to predict the peak strength of each of the specimens. Additionally, moment capacity equations by Griffith and Vaculik were applied adopting the ultimate torsional shear stress relationships derived from torsional shear testing ($SC_{GV\tau}$, $w_{GV\tau}$). For these calculations summarized in Table 7, a much simpler yet mathematically equivalent form of Eq. (5) (provided in AS 3700) applicable for typical failure mechanisms listed in Fig. 8 was utilized:

$$w = \frac{2a_f}{L_d^2}(k_1 M_h + k_2 M_d) \tag{8}$$

Here, w is the uniformly applied wall face pressure; M_h and M_d again denote moment capacities associated with horizontal and diagonal bending per unit crack length; L_d is the effective length of the wall which depends on its boundary conditions and presence and absence of an opening; k_1, k_2 and a_f are coefficients dependent on the associated failure mechanism (Formulae for calculating k_1, k_2 and a_f are provided in a tabular form based on support conditions and presence/absence of openings for standard mechanisms of Fig. 8 in AS 3700 [47]). The values of these coefficients corresponding to the specimens have been provided in Table 7.

Table 6
Moment capacities obtained adopting theoretical and experimental ultimate shear stress relationships (critical values in bold).

Moment Capacity (per unit crack length) [kNm/m]	$\tau_u = 0.9\sigma + 1.6 f_{mt}$ [48]			Experimental τ_u		
	CS τ_u [MPa] = 0.9σ + 1.52		Clay τ_u [MPa] = 0.9σ + 0.66	CS τ_u [MPa] = 1.14σ + 1.81		Clay τ_u [MPa] = 1.55σ + 1.07
	CS-005-RR	CS-000-RF CSW-000-RF CAV-000-RF (CS)	CL-000-RF CAV-000-RF (CL)	CS-005-RR	CS-000-RF CSW-000-RF CAV-000-RF (CS)	CL-000-RF CAV-000-RF (CL)
M_h (line failure)	**1.97**	**1.98**	5.22	**1.97**	**1.98**	5.22
M_h (stepped failure)	4.82	4.68	**2.52**	5.75	5.58	**4.13**
M_d	**1.33**	**1.28**	**0.55**	**1.45**	**1.39**	**0.63**

Table 7
Analytical predictions of peak strength of specimens by virtual work based methods.

Specimen	*HE* [#]	*VE* [#]	*Op* [–]	L_d [m]	H_d [m]	α [–]	a_f [–]	k_1 [–]	k_2 [–]	SC_{GV} [–]	w_{GV} [kPa]	SC_{AS} [–]	w_{AS} [kPa]	$SC_{GV\tau}$ [–]	$w_{GV\tau}$ [kPa]	SC_{exp} [–]	w_{exp} [kPa]
CS-005-RF	2	2	n	1.99	1.38	1.06	1.54	0.50	2.88	2.05	3.76	2.24	4.12	2.18	4.06	2.00	3.70
CS-000-RF	1	2	n	1.99	2.75	0.53	1.21	0.97	1.52	1.29	2.37	2.07	3.79	1.34	2.9	1.44	2.65
CSW-000-RF*	1	1	n	1.54	2.75	0.41	1.16	0.50	1.18	1.32	2.43	1.90	3.49	1.39	2.58	1.27	1.38
CSW-000-RF	1	2	y	1.54	2.75	0.41	0.56	0.50	1.18	0.64	1.18	0.92	1.69	0.67	1.25	1.27	2.34
CL-000-RF	1	2	n	2.01	2.76	0.40	1.15	1.10	1.73	1.11	2.13	1.35	2.60	1.67	3.37	1.72	3.30
CAV-000-RF CS	1	2	n	1.99	2.75	0.53	1.21	0.97	1.52	1.29	2.37	2.07	3.79	1.35	2.49	1.29	2.43
CAV-000-RF CL	1	2	n	2.19	2.72	0.44	1.17	1.06	1.90	0.95	1.83	1.13	2.18	1.41	2.84		

HE and ***VE*** indicate the number of restrained horizontal and vertical edges respectively.
Op indicates presence (y) or absence (n) of an opening in the analytical idealization.
SC and ***w*** denote shear coefficient and wall face pressure respectively (Eqs. (2) and (8)).

k_1 also takes into account the percentage of moment capacity arising from horizontal bending at the return wall connections that contributes to the peak strength of walls and is considered here as 50%. This is as per the recommendation by Griffith and Vaculik [45] based on the observation that peak strength corresponds to attainment of full moment capacity only in diagonal cracks and approximately half moment capacity in vertical cracks developing at the connection of the OOP with the return walls due to horizontal bending.

Considering the large area of the opening and the localization of damage in the longer panel (reported in Section 4.2.3), a further configuration in addition to the standard one was considered for the specimen with the opening. The CSW-000-RF analytical prediction (as recommended by AS 3700 [47]) considers the whole wall with the opening and both vertical edges restrained while CSW-000-RF* considers only the longer panel with one of the vertical edges kept free. Additionally, the peak strength of the cavity-wall specimen CAV-000-RF was calculated as the sum of the strength of the individual leaves. The results of these analytical calculations are compared to experimental results in Fig. 17.

Predictions of strength computed using the moment capacity equations proposed by Griffith and Vaculik [45] (SC_{GV}) as well as with the same equations but assuming experimentally derived ultimate torsional shear stress relationships ($SC_{GV\tau}$) were very good. AS 3700 overpredicts the wall strength in 4 out of 6 cases. A marked improvement in $SC_{GV\tau}/SC_{Exp}$ ratio compared to SC_{GV}/SC_{Exp} ratio was observed especially in case of specimens CL-000-RF and CAV-000-RF in which failure occurred by stepped cracks (*i.e.* clay leaf of CAV-000-RF) whose moment capacities are governed by the ultimate torsional shear stress occurring in bed-joints instead of line cracks. For both these specimens, the peak strength is underpredicted, highlighting the requirement for more detailed evaluation of the relationship defining the ultimate torsional shear stress in a bed joint. In case of CSW-000-RF, a higher strength which is also closer to the experimentally measured peak strength is obtained while considering only the longer segment (CSW-000-RF* in Fig. 17) rather than the full panel with opening (CSW-000-RF in Fig. 17). Despite the very low deviation seen from experimental results in case of CSW-000-RF*, the observed failure mechanism was quite different from typical failure mechanisms considered in these analytical methods. Another interesting observation is that the experimental CAV-000-RF *SC* was lower than *SC*s related to the single-leaf specimens (CS-000-RF and CL-000-RF). This confirms the lower shear coefficient of cavity walls with respect to single leaf walls which was also observed in the case of vertically spanning walls subjected to one-way-bending [7].

5.3. Experimental-based application of VW method (EVW)

The codified form of the VW method (Eq. (8)) provides a very user-friendly and simplified procedure to predict the strength of walls in OOP panels in two-way bending with good accuracy. However, limitations may arise from the fact that the codified form of the method is reliable only for standard failure mechanisms (Fig. 8), for which the coefficients associated with Eq. (8) can be calculated. Consequently, explicit application of the VW method outlined in Section 5.1 (Eqs. (3)-(7)) based on experimental observations was carried out for each of the specimens considering the

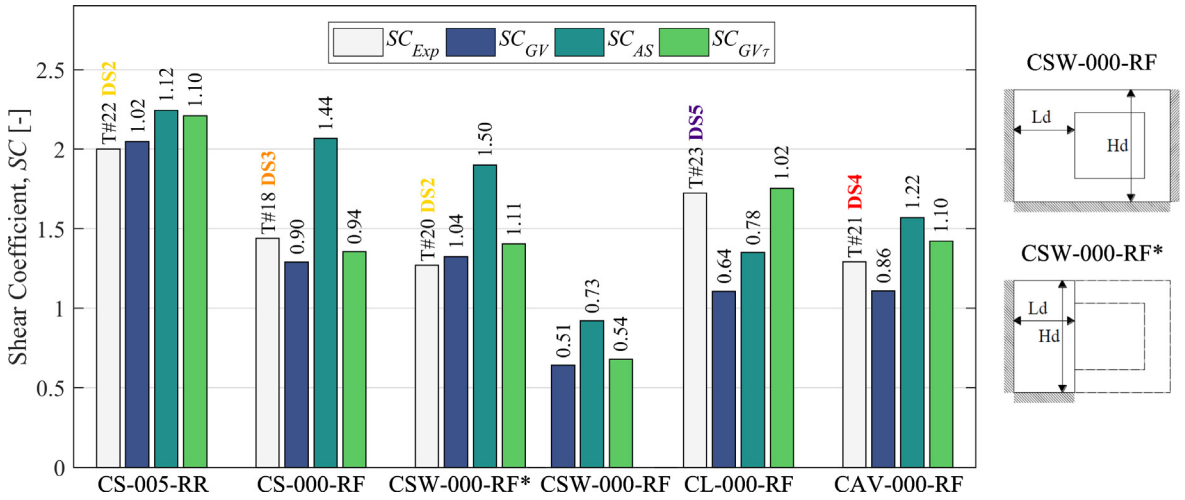

Fig. 17. *SC* evaluated experimentally and analytically (along vertical axis) and ratio of *SC*'s to *SC* evaluated experimentally (on top of each bar). Schematic representation of different scenarios assumed for CSW-000-RF.

actual crack patterns that were documented after the experiments to evaluate the reliability of the codified VW method.

A simple way to explicitly apply the VW method is to discretize the observed failure mechanisms into building blocks of known geometrical configuration, such as pyramids and wedges based on the exhibited cracks and deformed shapes (Fig. 18). Control displacement for the specimens is reasonably assumed to be occurring at the location of measured peak displacements. It is to be noted that these elements were used not only to discretize the global deflected shapes but also to derive the rotations associated with diagonal, horizontal and vertical cracks. Crack rotations along with associated moment capacities (Eqs. (6) and (7)) are used to calculate the internal work of the system as per Eq. (4). The contribution of horizontal cracks to the specimen capacity was neglected on the basis of recommendations of Vaculik [35].

A control displacement of Δ_c (assumed to be equal to unity) at the locations seen in Fig. 18, corresponds to a displaced volume of $LH/3$ and $LH/2$ for pyramid and wedge elements, respectively. These displaced volumes were used for the calculation of external work and ultimately the wall strength using Eqs. (3) and (5), respectively. Details about the EVW method performed are provided here only for specimens CS-005-RR and CSW-000-RF.

For CS-005-RR and CSW-000-RF, crack patterns and deformed shapes corresponding to Test #22 and #20 (Figs. 9 and 11) respectively were considered for the computation of the ultimate strength. The discretization in pyramid and wedge elements of the deflected shapes adopted for both walls are provided in Fig. 19. Control displacements were assumed at the point of intersection of the diagonal cracks and vertical line crack for CS-005-RR and along the vertical crack propagating from the opening of CSW-000-RF. The adopted discretization of the specimens into pyramids and wedge elements showed a very good agreement with experimentally measured displaced volume (Fig. 20). Such observations also confirm that during the attainment of peak strength, the OOP panel can be reasonably considered to be behaving as a set of rigid blocks, to which the method of virtual work can be very reliably applied. Although pyramid elements are assumed for the computation of the displaced volume (see deflected shapes of Figs. 9b and 11b), no diagonal cracks on elements P1, P4 for CS-005-RR and also element P1

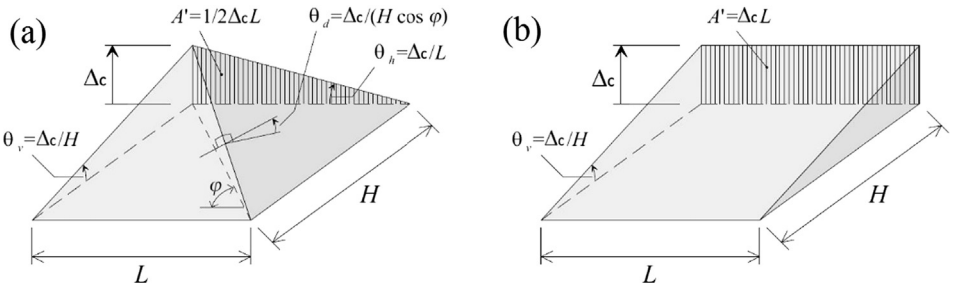

Fig. 18. Rectangular elements into which OOP panels were divided into along with their geometrical properties: pyramid (a) and wedge (b). For the elements of dimension $L{\cdot}H$, θ_d, θ_h and θ_v denote crack rotations associated with diagonal, horizontal and vertical cracks respectively [35].

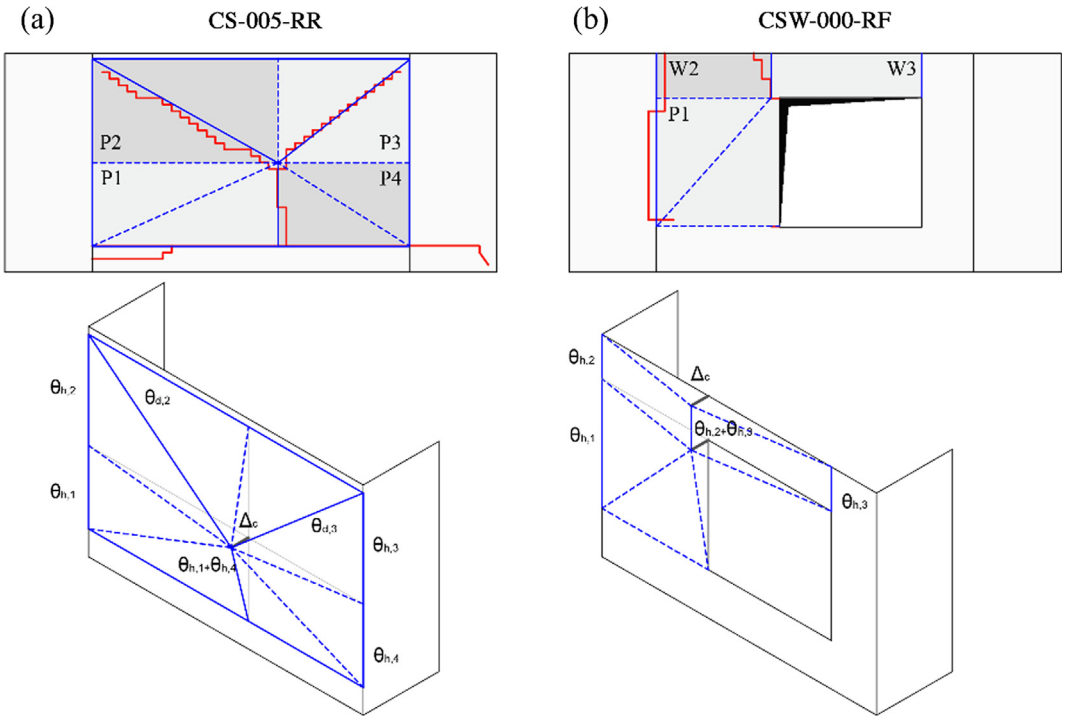

Fig. 19. Comparison between observed crack pattern and discretization adopted for CS-005-RR (Test #22) (a) and CSW-000-RF (Test #20) (b): P-Pyramid, W-Wedge, Δ_c: assumed control displacement and θ_h, θ_d: considered crack rotations.

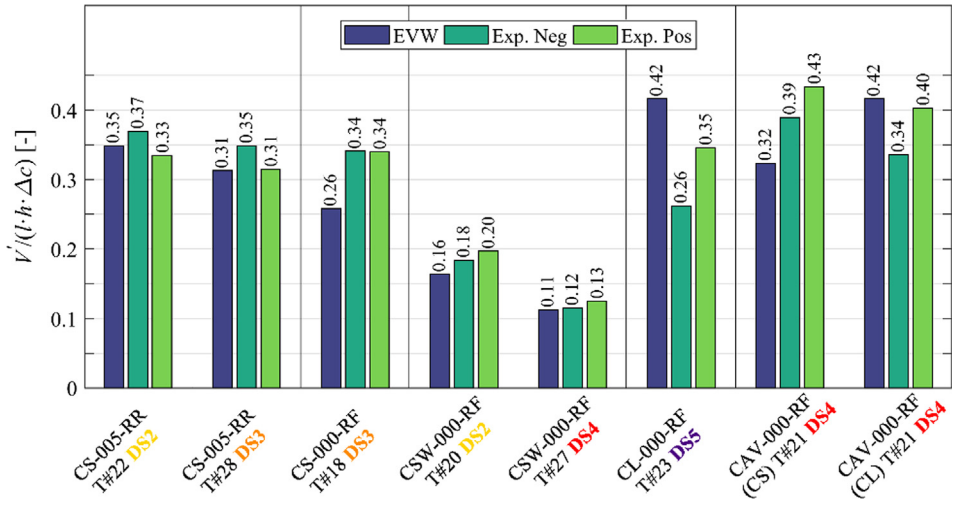

Fig. 20. Comparison of displaced volume calculated using discretization adopted for EVW and experimentally measured (for all deflected shapes presented in Section 4.2).

(for CSW-000-RF) were observed (Fig. 19). Consequently, contribution to internal work along these diagonals (dashed lines in Fig. 19) was not considered. In case of CSW-000-RF, the crack at the connection with the left return wall was observed to have already developed completely by Test #20: full cracking moment (unlike 50% of cracking moment assumed in the codified VW method) was assumed while calculating internal work. Comparisons of results of peak strength obtained from EVW and the codified approach implemented in Section 5.2, both using the same moment capacity equations and measured ultimate torsional shear strength of the bed joint (Table 6) with experimental results is provided in Fig. 21. It is observed that SC_{EVW} can be lower than $SC_{GV\tau}$. Such differences arise due to the fact that horizontal cracks occurred for some specimens instead of diagonal cracks as predicted by standard mechanisms assumed by the codified VW method ($SC_{GV\tau}$.). The contribution of horizontal cracks to the peak strength of the wall is neglected in both SC_{EVW} and $SC_{GV\tau}$ while that of diagonal cracks is not, leading to higher $SC_{GV\tau}$ values with respect to SC_{EVW}. These deviations also arise due to geometric differences (e.g. length and inclination of diagonal cracks φ) between the assumed standard failure mechanisms by the codified approach with respect to the experimental failure mechanisms.

The calculations reported in this section of the paper represent an exercise performed towards assessing the reliability of the VW method as well as the most important input information that goes into it for correctly assessing the OOP strength of a wall. Such factors could not be evaluated in the predictive methods implemented in Section 5.2 because of the large number of assumptions inherent in the codified approach, notably the pre-assigned standard failure mechanism on the basis of the geometric configuration and boundary conditions of the wall. The internal work and evolution of displaced volume calculated while doing this exercise are also interesting with the target of deriving SDOF models for the tested walls and to study their behaviour at higher damage states *i.e.* their post-peak behavior (Fig. 20). However, for all specimens tested other than CSW-000-RF, the failure mechanisms implicitly associated as well as the peak strengths estimated by the codified approach were quite accurate, especially when using moment capacity expressions developed by Griffith and Vaculik [45] along with experimentally derived torsional shear strength relationships. Considering the accuracy achieved despite the simplicity of the calculations, such analytical approaches present strong potential for assessment as well as design calculations.

It is to be noted that the shear coefficients calculated using analytical approaches are sometimes lower than the experimentally observed value for some specimens. It is believed that this is the result of assumptions inherent in all forms of analytical methods used in this paper: most significantly, while moment capacities of all diagonal and vertical cracks are reached simultaneously, the resistance provided by horizontal cracks to peak strength is

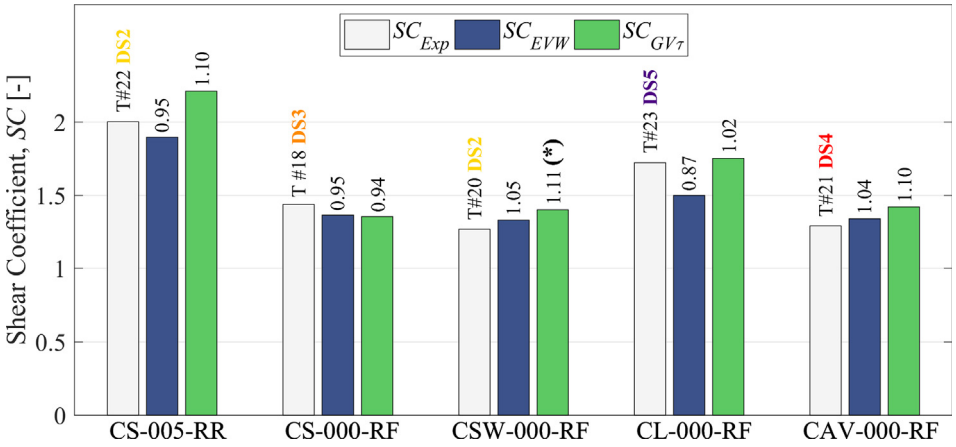

Fig. 21. Comparison of shear coefficients calculated using EVW and the codified approach with experimental results (* = CSW-000-RF*).

neglected and the variability of the material in a wall is not taken into account, as mean values of material properties are used in the analytical calculations.

6. Concluding remarks

This paper presents the results of a two-way bending OOP shaking table test on five U-shaped full-scale URM single leaf and cavity wall specimens. The test setup allowed testing of the specimens under different loading and boundary conditions, assuming second-floor accelerograms as dynamic input motion. The evolution of the fundamental period of the specimens was monitored along the testing sequence.

Acceleration capacities associated with all specimens was very high. In particular, structural damage was observed for the specimen restrained on all four edges at a *PTA* of 1.93 g and for the four specimens free on top above 1.28 g. Calcium silicate specimens exhibited a rather brittle behaviour characterized by peak strengths achieved at very low level of displacements. After peak strength was achieved, the specimens also showed very quick degradation of both strength and stiffness occurring over a short range of displacements. However, the wall restrained on all four edges presented a comparatively higher residual capacity due to the combined action of higher axial force and top horizontal restraint. Clay masonry instead showed a better performance: higher lateral load carrying capacity was sustained over a wider range of displacements. Higher residual strength was also observed for this specimen. Such differences in behaviour can be attributed to the predominant failure mechanism under horizontal bending characterizing the two types of masonry. Line failure which was widely observed in the calcium silicate specimens is controlled by the flexural tensile strength of the units and is usually associated with a poor residual capacity. On the other hand, stepped failure largely observed in clay masonry and associated with a moment capacity comparable to that observed in line failure provides significant residual capacity by virtue of torsional shear response of the bed joints. Predominance of line failure in calcium silicate walls also resulted in the failure mechanisms slightly different from those reported widely in literature. The tests also confirmed the higher OOP vulnerability of cavity walls with respect to single leaf walls in terms of wall shear coefficient which had also been observed in the case of vertically spanning walls subjected to one-way-bending.

The paper also presents a characterization test to evaluate the torsional shear capacity of bed joints. This is also a controlling parameter in currently existing state of the art analytical formulation for predicting the strength of URM walls under OOP two-way bending. While the method codified in AS 3700 overestimates wall strengths (especially for CS specimens), good agreement with experimental results is shown by the formulation proposed by Griffith and Vaculik [45]. The results of the latter method improve when the value of ultimate shear stress occurring in a bed joint adopted for calculating moment capacity associated with horizontal and diagonal bending is modified based on the results of this characterization test, especially in case of specimens showing stepped failure. It is interesting to note that the application of these methods for the purpose of assessing wall strengths used coefficients which have been derived for standard mechanisms reported in literature, which did not necessarily occur.

The virtual work method, which forms the underlying principle of this analytical formulation, was also explicitly applied taking into account experimentally observed cracking patterns and deformed shapes. Excellent agreement was achieved with experimental results, indicating the virtual work method (utilizing moment capacity equations developed by Griffith and Vaculik [45] and adopting the experimentally evaluated torsional shear strength of bed joints) as a robust methodology to study the OOP behaviour of URM.

All experimental data reported in this article along with detailed descriptions and illustrations of instrumentation adopted for each of the specimens are freely available upon request from www.eucentre.it/nam-project. This data along with other information [7] already made available within the framework of the same project presents an opportunity for researchers to calibrate numerical models or study scenarios not explicitly considered in the context of this article for the behaviour of URM under OOP loading.

Conflict of interest

The authors declare that there is no conflict of interest.

Acknowledgements

This paper describes an activity that is part of the “Study of the vulnerability of masonry buildings in Groningen” project at the EUCENTRE, undertaken within the framework of the research program for hazard and risk of induced seismicity in Groningen sponsored by the Nederlandse Aardolie Maatschappij BV. The authors would like to thank all the parties involved in this project, namely EUCENTRE and University of Pavia (DICAr) laboratories that performed the tests, NAM, Arup and TU Delft. The valuable advice of R. Pinho, A. Penna and M. Griffith is gratefully acknowledged. Thanks go also to J. Uilenreef, F. Dacarro, S. Peloso, M. Mandirola, A. Fragomeli, M. P. Scovenna and G. Sinopoli for the practical support. The authors would also like to thank the anonymous reviewers for their comments, which certainly contributed to an improvement of the manuscript.

References

[1] A.W. Page, The Newcastle earthquake - behaviour of masonry structures, Mason Int. 5 (1991) 11–18.
[2] C. Oyarzo-Vera, M.C. Griffith, The Mw 6.3 Abruzzo (Italy) earthquake of April 6th, 2009: on site observations, Bull. New Zeal. Soc. Earthq. Eng. 42 (4) (2009) 302–307.
[3] D. D'Ayala, E. Speranza, Definition of collapse mechanisms and seismic vulnerability of historic masonry buildings, Earthq. Spectra 19 (3) (2003) 479–509, https://doi.org/10.1193/1.1599896.
[4] A. Penna, P. Morandi, M. Rota, C.F. Manzini, F. da Porto, G. Magenes, Performance of masonry buildings during the Emilia 2012 earthquake, Bull. Earthq. Eng. 12 (5) (2014) 2255–2273, https://doi.org/10.1007/s10518-013-9496-6.
[5] L. Moon, D. Dizhur, I. Senaldi, et al., The demise of the URM building stock in Christchurch during the 2010–2011 Canterbury earthquake sequence, Earthq. Spectra 30 (1) (2014) 253–276, https://doi.org/10.1193/022113EQS044M.
[6] M.C. Griffith, N.T.K. Lam, J.L. Wilson, K. Doherty, Experimental investigation of unreinforced brick masonry walls in flexure, J. Struct. Eng. 130 (3) (2004) 423–432, https://doi.org/10.1061/(ASCE)0733-9445(2004) 130:3(423).
[7] F. Graziotti, U. Tomassetti, A. Penna, G. Magenes, Out-of-plane shaking table tests on URM single leaf and cavity walls, Eng. Struct. 125 (2016), https://doi.org/10.1016/j.engstruct.2016.07.011.
[8] O. Penner, K.J. Elwood, Out-of-plane dynamic stability of unreinforced masonry walls in one-way bending: shake table testing, Earthq. Spectra 32 (3) (2016) 1675–1697, https://doi.org/10.1193/011415EQS009M.
[9] C.C. Simsir, M.A. Aschheim, D.P. Abrams, Out-of-plane dynamic response of unreinforced bearing walls attached to flexible diaphragms, in: Proc 13th World Conf Earthq Eng, 2045, 2004, p. 15.
[10] M. Giaretton, D. Dizhur, J.M. Ingham, Dynamic testing of as-built clay brick unreinforced masonry parapets, Eng. Struct. 127 (2016) 676–685, https://doi.org/10.1016/j.engstruct.2016.09.016.
[11] K. Beyer, M. Tondelli, S. Petry, S. Peloso, Dynamic testing of a four-storey building with reinforced concrete and unreinforced masonry walls: prediction, test results and data set, Bull. Earthq. Eng. 13 (10) (2015) 3015–3064, https://doi.org/10.1007/s10518-015-9752-z.
[12] N.T.K. Lam, M. Griffith, J. Wilson, K. Doherty, Time-history analysis of URM walls in out-of-plane flexure, Eng. Struct. 25 (6) (2003) 743–754, https://doi.org/10.1016/S0141-0296(02)00218-3.
[13] L. Sorrentino, R. Masiani, M.C. Griffith, The vertical spanning strip wall as a coupled rocking rigid body assembly, Struct. Eng. Mech. 29 (4) (2008) 433–453, https://doi.org/10.12989/sem.2008.29.4.433.

[14] U. Tomassetti, F. Graziotti, A. Penna, G. Magenes, Modelling one-way out-of-plane response of single-leaf and cavity walls, Eng. Struct. 167 (2018) 241–255, https://doi.org/10.1016/j.engstruct.2018.04.007.
[15] M.C. Griffith, J. Vaculik, N.T.K. Lam, J. Wilson, E. Lumantarna, Cyclic testing of unreinforced masonry walls in two-way bending, Earthq. Eng. Struct. Dyn. 36 (6) (2007) 801–821, https://doi.org/10.1002/eqe.654.
[16] F. Messali, G. Ravenshorst, R. Esposito, J.G. Rots, Large-scale testing program for the seismic characterization of Dutch masonry walls, in: 16th World Conf Earthq. 2017; June): Paper No. 4753. https://repository.tudelft.nl/islandora/object/uuid%3A7f4baaa0-b1d4-49ad-b41c-584f324c102e.
[17] H. Derakhshan, W. Lucas, P. Visintin, M.C. Griffith, Out-of-plane strength of existing two-way spanning solid and cavity unreinforced masonry walls, Structures 13 (2018) 88–101, https://doi.org/10.1016/j.istruc.2017.11.002.
[18] L.F. Restrepo-Vélez, G. Magenes, M.C. Griffith, Dry stone masonry walls in bending - Part I: Static tests, Int. J. Archit. Herit. 8 (1) (2014) 1–28, https://doi.org/10.1080/15583058.2012.663059.
[19] J. Vaculik, M.C. Griffith, Out-of-Plane Shaketable Testing of Unreinforced Masonry Walls in Two-Way Bending, Springer, The Netherlands, 2018. https://doi.org/10.1007/s10518-017-0282-8.
[20] D. Dizhur, J. Ingham, Seismic Improvement of Loadbearing Unreinforced Masonry Cavity Walls, Report - Branz ER3, New Zealand, 2015.
[21] F. Graziotti, A. Rossi, M. Mandirola, A. Penna, G. Magenes, Experimental characterisation of calcium-silicate brick masonry for seismic assessment, in: Proceedings of the 16th International Brick and Block Masonry Conference, 2016, pp. 1619–1627, https://doi.org/10.1201/b21889-215.
[22] F. Graziotti, U. Tomassetti, S. Kallioras, A. Penna, G. Magenes, Shaking table test on a full scale URM cavity wall building, Bull. Earthq. Eng. 15 (12) (2017), https://doi.org/10.1007/s10518-017-0185-8.
[23] S. Kallioras, G. Guerrini, U. Tomassetti, et al., Experimental seismic performance of a full-scale unreinforced clay-masonry building with flexible timber diaphragms, Eng. Struct. 161 (2018) 231–249, https://doi.org/10.1016/j.engstruct.2018.02.016.
[24] U. Tomassetti, A.A. Correia, P.X. Candeias, F. Graziotti, A. Campos Costa, Two-way bending out-of-plane collapse of a full-scale URM building tested on a shake table, Bull. Earthq. Eng. (2018) (accepted for publication).
[25] A.A. Correia, U. Tomassetti, A. Campos Costa, A. Penna, G. Magenes, F. Graziotti, Collapse shake-table test on a URM-timber roof structure, in: 16th European Conference on Earthquake Engineering, 2018.
[26] F. Graziotti, A. Penna, G. Magenes, A comprehensive in-situ and laboratory testing programme supporting seismic risk analysis of URM buildings subjected to induced earthquakes, Bull. Earthq. Eng. (2018), https://doi.org/10.1007/s10518-018-0478-6.
[27] NPR 9998:2017: Assessment of buildings in case of erection, reconstruction and disapproval - Basic rules for seismic actions: Induced earthquakes, Netherlands Standardization Institute (NEN), Delft, The Netherlands, 2017.
[28] EN, 1052-1, Methods of test for masonry – Part 1: Determination of compressive strength Brussels, European Standards, Belgium, CEN/TC 1998.
[29] EN, 1052-5, Methods of test for masonry – Part 5: Determination of bond strength by the bond wrench method 2005 European Standards, CEN/TC Brussels, Belgium.
[30] EN, 1015-11, Methods of test for mortar for masonry – Part 11: Determination of flexural and compressive strength of hardened mortar 1999 European Standards, CEN/TC Brussels, Belgium.
[31] EN 772-1, Methods of test for masonry units – Part 1: Determination of compressive strength. European Standards, CEN/TC, Brussels, Belgium, 2011.
[32] EN, 1052-3, Methods of test for masonry – Part 3: Determination of initial shear strength, European Standards, Brussels, Belgium, CEN/TC 2002.
[33] G. Skroumpelou, F. Messali, R. Esposito, J.G. Rots, Mechanical characterization of wall tie connection in cavity walls, in: 10th Australian Masonry Conference, Sydney Australia, 2018.
[34] W. Samarasinghe, S.J. Lawrence, Behaviour of masonry under combined torsion and compression, Calgary, Canada, 1994.
[35] J. Vaculik, Unreinforced masonry walls subjected to out-of-plane seismic actions PhD. Thesis, University of Adelaide, Australia, 2012.
[36] S.P. Timoshenko, D.H. Young, Elements of Strength of Materials, fourth ed., Van Nostrand, New York, 1962.
[37] U. Tomassetti, L. Grottoli, S. Sharma, F. Graziotti, Dataset from the dynamic shake-table testing of five full-scale single leaf and cavity URM walls subjected to out-of-plane two-way bending, Data in Brief (2018) (submitted for publication).
[38] S. Sharma, U. Tomassetti, L. Grottoli, F. Graziotti, Out-of-Plane Two-Way Bending Shaking Table Tests on Single Leaf and Cavity Walls, Technical Report: EUC137/2018U, EUCENTRE, Pavia, Italy, 2018.
[39] S. Lagomarsino, A. Penna, A. Galasco, S. Cattari, TREMURI program: an equivalent frame model for the nonlinear seismic analysis of masonry buildings, Eng. Struct. 56 (2013) 1787–1799, https://doi.org/10.1016/j.engstruct.2013.08.002.
[40] S. Kallioras, F. Graziotti, A. Penna, Numerical assessment of the dynamic response of a URM terraced house exposed to induced s eismicity, Bull. Earthq. Eng. (2018) 39, https://doi.org/10.1007/s10518-018-0495-5.
[41] J.J. Bommer, H. Crowley, R. Pinho, B. Polidoro, Selection of Acceleration Time-Series for Shake Table Testing of Groningen Masonry Building at the EUCENTRE, Pavia, Report - Groningen Field Seismic Hazard and Risk Assessment Project, Pavia, Italy, 2015.
[42] R. Brincker, L. Zhang, P. Andersen, Modal identification from ambient responses using frequency domain decomposition, in: Proceedings of the 18th International Modal Analysis Conference, 2000, pp. 625–630.
[43] E.L. Wilson, K.J. Bathe, F.E. Peterson, H.H. Dovey, SAP - a structural analysis program for linear systems, Nucl. Eng. Des. 25 (2) (1973) 257–274, https://doi.org/10.1016/0029-5493(73)90048-4.
[44] EUCENTRE, URM, walls in out-of-plane two way bending (YouTube playlist) Published 2017 www.youtube.com/watch?v=WvYS91br9HQ&list=PLRDMVFxhFvQnMRn7SDXreqbcg044logeB.
[45] M.C. Griffith, J. Vaculik, Out-of-plane flexural strength of unreinforced clay brick masonry walls, Mason Soc. J. 25 (1) (2007) 53–68.
[46] S. Lawrence, R. Marshall, Virtual work design method for masonry panels under lateral load, in: 12th IBMAC, Madrid, Spain, 2000.
[47] AS 3700-2001:Masonry Structures, Australian Standard, Sydney, Australia, 2001.
[48] C. Willis, Design of unreinforced masonry walls for out-of-plane loading PhD. Thesis, University of Adelaide, Australia, 2004.